1,3-Diradicals Embedded in Curved Paraphenylene Units: Singlet *versus* Triplet and In-plane Aromaticity

Yuki Miyazawa,[†] Zhe Wang,[†] Misaki Matsumoto,[†] Sayaka Hatano,[†] Ivana Antol,[‡]* Eiichi Kayahara,[§] Shigeru Yamago,[§]* and Manabu Abe[†]*

[†]Department of Chemistry, Graduate School of Science, Hiroshima University, 1-3-1 Kagamiyama, Higashi-Hiroshima, Hiroshima 739-8526, Japan

mabe@hiroshima-u.ac.jp

[‡]Laboratory for Physical Organic Chemistry, Division of Organic Chemistry and Biochemistry, Ruđer Bošković Institute, Bijenička cesta 54, 10000 Zagreb, Croatia

Ivana.Antol@irb.hr

[§]Institute for Chemical Research, Kyoto University, Uji, Kyoto 611-0011, Japan

yamago@scl.kyoto-u.ac.jp

Abstract

Curved π-conjugated molecules and open-shell structures have attracted much attention from the perspective of fundamental chemistry, as well as materials science. In this study, the chemistry of 1,3-

diradicals (**DR**s) embedded in curved cycloparaphenylene (**CPP**s) structures, **DR**-(*n*+3)**CPP**s (*n* = 0-4), was investigated to understand the effects of the curvature and system size on the spin–spin interactions, singlet *versus* triplet, as well as their unique characteristics such as in-plane aromaticity. A triplet ground state was predicted for the larger 1,3-diradicals, such as the seven- and eight-paraphenylene-unit-containing diradicals, **DR-7CPP** (*n* = 4) and **DR-8CPP** (*n* = 5), by quantum chemical calculations. The smaller sized diradicals **DR**-(*n*+3)**CPP**s (*n* = 0-3) were found to possess their singlet ground states. Thus, the ground state spin multiplicity is controlled by the size of the paraphenylene cycle. The size effect on the ground state spin-multiplicity was confirmed by the experimental generation of **DR-6CPP** in the photochemical denitrogenation of its azo-containing precursor (**AZ-6CPP**). Intriguingly, a unique type of in-plane aromaticity emerged in the smaller sized singlet-states such as S-**DR-4CPP** (*n* = 1), as proven by the nucleus-independent chemical shift calculations (NICS) and analysis of the anisotropy of the induced current density (ACID), which demonstrate that homoconjugation between the 1,3-diradial moiety arises because of the curved and distorted bonding system.

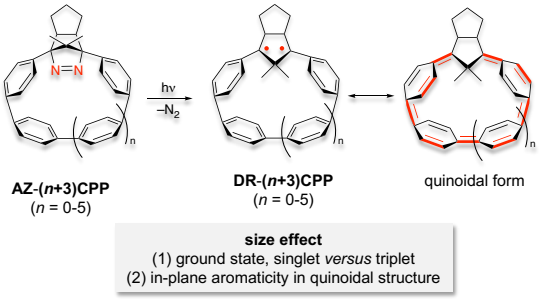

削除: 4

Introduction

In the last decade, open-shell molecules have attracted considerable attention not only in the field of reactive intermediates but also in materials science. For example, radical-based light emitting diodes have been developed using isolatable triaryl methyl radicals,[1,2,3] magnetically robust high-spin molecules have been developed using new molecular designs,[4,5] and a new bonding system, π single bonding, has emerged through research into localized diradicals.[6–13] Furthermore, the isolation of singlet diradicaloids such as Tchitchibabin derivatives has revealed their singlet fission behavior and non-linear optical character, and these are now hot topics in π-conjugated materials.[7,14–24] To date, we have investigated localized 1,3-diradicals **DR** (see Figure 1a), which are key intermediates in bond-homolysis.[25–28,29] The ground state spin-multiplicity is typically controlled by the substituents at the C2 position, and the triplet ground state for **DR** having X = H and CH_3 can be switched to a singlet ground state by the introduction of electron-donating and electron-withdrawing substituents, for example, X = F, OR, and SiR_3 (Figure 1a).[12,30]

書式を変更：上付き

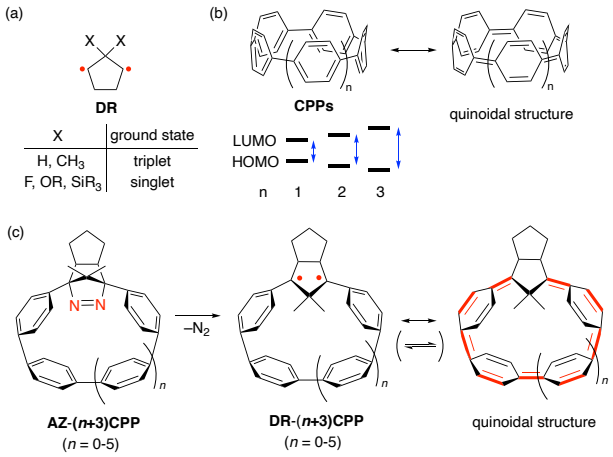

Figure 1. Substituent effects on the ground-state spin-multiplicity of cyclopentane-1,3-diyl diradicals (a). Effect of size on the quinoidal character of cycloparaphenylenes (b). This study (c).

In the late 2000's, pioneering studies in the synthesis of a new series of π-conjugated molecules, cycloparaphenylenes (CPPs), were reported; since then, these intriguing molecules have attracted much attention.[31,32,33] The most striking feature of these hoop-shape molecules is the hypsochromic shift of the HOMO–LUMO energy gap with increasing number of benzene rings in the CPP structures (Figure 1b).[34,35,36] This behavior is totally opposite to that of linear paraphenylenes. This unique behavior is rationalized as being a result of the quinoidal contribution of the small CPPs arising from the diradical character induced by the curved structure of the benzene rings.[37] In the present study, we designed diradicals **DR-(*n*+3)CPPs** to investigate the quinoidal character in the hoop-shaped structures (Figure 1c). Among the precursors **AZ-(n+3)CPPs** featuring curved paraphenylene units, a novel azoalkane **AZ-6CPP** ($n = 3$) was synthesized to investigate its electronic

削除: able to be

character and the corresponding chemistry of diradical **DR-6CPP** (n = 3). Furthermore, quantum chemical calculations were carried out for all diradicals **DR-(*n*+3)CPP** (n = 0–5) to understand the experimental results on **DR-6CPP**, and the effect of the ring size on the diradical chemistry in the hoop-shaped structure. In particular, we draw attention to the size effect on the ground state spin multiplicity (singlet (S) *versus* triplet (T)) and interaction of the two spins with the curved π-electron system (quinoidal structure).

Results

Synthesis of AZ-6CPP. The synthetic route to **AZ-6CPP** is shown in Scheme 1. Double lithium–bromide exchange of compound **1** and its addition to 4,4-dimethoxycyclohexan-2,5-dien-1-ones (**2**) gave diketal intermediate **3**. Subsequent acid hydrolysis produced diketone **4**.[38] The double arylation of **4** using (4-bromophenyl)lithium produced a diol, followed by dimethylation using NaH and MeI to afford dibromide **5** in 13% yield (four steps). The Yamamoto coupling of the dibromide followed by the reductive aromatization[31] of **6** afforded **AZ-6CPP** in approximately 1% total yield based on the starting material. Single crystals were obtained by the gradual evaporation of a mixture of $CHCl_3$ and MeOH, and the strained structure was confirmed by X-ray crystallographic analysis (Figure 2a). Two **AZ-6CPP** molecules were found in a single crystal lattice, and, in this structure, a molecule of $CHCl_3$ occupies the curved paraphenylene unit. In the ^{1}H-NMR spectrum (*vide infra*), the two CH_3 groups appeared at δ = –2.36 and –0.49 ppm relative to the signal of benzene (δ = 7.16 ppm).

The high-field resonance is a result of the aromatic ring current induced by the benzene rings in the macrocyclic structure. The dimethyl group was found to be *trans*-configured relative to the cyclopentane ring. The bond lengths, average torsion angles (θ = 17.2°) and bending of the benzene rings (α = 17.7°) of the paraphenylene units of **AZ-6CPP** were compared with those of *p*-sexiphenyl, a linear paraphenylene C_6H_5-$(C_6H_4)_4$-C_6H_5 (Figure 2b). Density functional theory (DFT) calculations at the B3LYP/6-31G(d) level of theory reproduced the molecular structure of **AZ-6CPP** well, although the torsion angles between the two benzene rings were computed to be slightly larger than those obtained in the X-ray analysis. The average torsion angle of curved **AZ-6CPP** (α = 17.7°) was found to be approximately half of that of *p*-sexiphenyl.

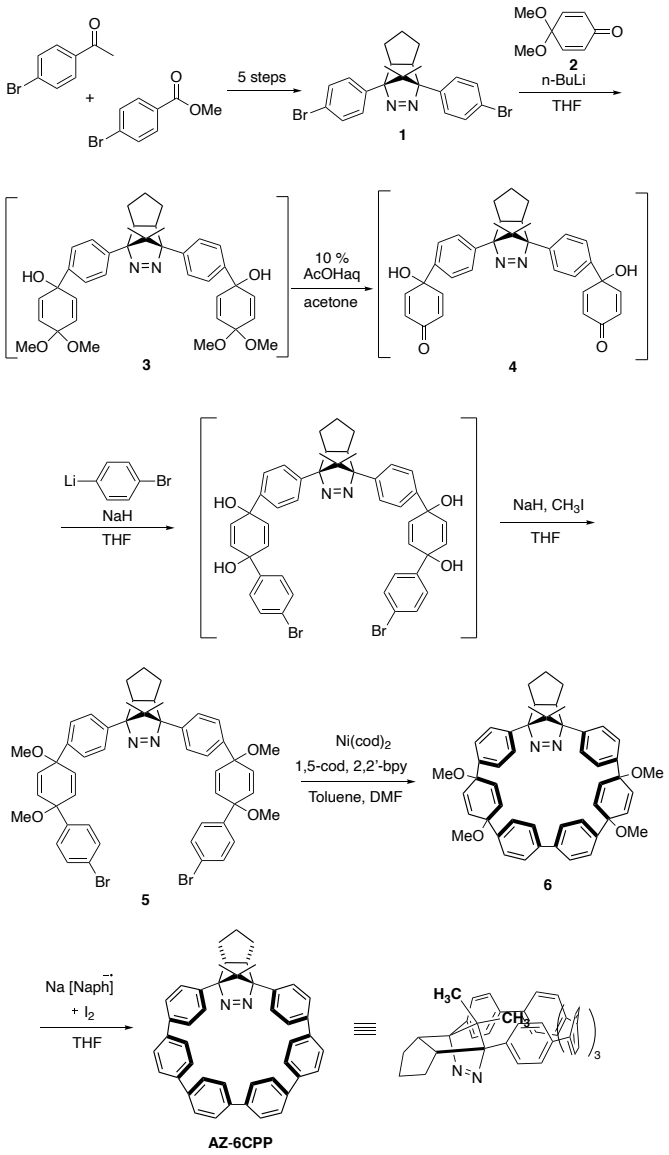

Scheme 1. Synthesis of **AZ-6CPP** (THF: tetrahydrofuran, cod: cyclooctadiene, DMF: dimethylformamide, bpy: bipyridine, and Naph: naphtalene).

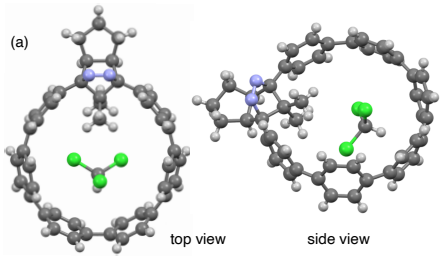

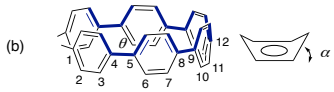

	X-ray analysis (B3LYP/6-31G(d))	
	AZ-6CPP	p-sexiphenyl
θ/°	17.2 (22.8)	(36.9)
α/°	17.7 (17.5)	(0.0)
C1-C2	1.391 (1.405)	(1.396)
C2-C3	1.386 (1.395)	(1.394)
C3-C4	1.399 (1.408)	(1.406)
C4-C5	1.493 (1.490)	(1.484)
C5-C6	1.402 (1.407)	(1.405)
C6-C7	1.386 (1.390)	(1.391)
C7-C8	1.401 (1.407)	(1.405)
C8-C9	1.494 (1.487)	(1.482)
C9-C10	1.397 (1.409)	(1.405)
C10-C11	1.382 (1.392)	(1.391)
C11-C12	1.403 (1.411)	(1.405)

Figure 2. (a) X-ray Structure of **AZ-6CPP** (black: carbon, gray: hydrogen, blue: nitrogen, and green: chloride). (b) Experimentally and computationally determined (at the B3LYP/6-31G(d) level of theory in parenthesis) torsion angles between the adjacent benzene-rings (θ, °), benzene bending angles (α, °), and bond lengths (Å) of the paraphenylene structures in **AZ-6CPP** and C_6H_5-$(CH_2)_4$-C_6H_5 (*p*-sexiphenyl).

Absorption and emission spectroscopy analysis of AZ-6CPP. The absorption and emission spectra of **AZ-6CPP** are shown in Figure 3. A broad absorption at approximately 400 nm (λ_{max} = 404 nm, ε = 7916 M^{-1} cm^{-1}) and a structured band at about 330 nm (λ_{max} = 331 nm, ε = 40509 M^{-1} cm^{-1}) were observed in the UV-vis absorption spectra (Figure 3a). The weak nπ* transition (ε ≈ 100 M^{-1}

cm^{-1}) of the azo chromophore (–N=N–) at approximately 360 nm seems to be hidden behind the strong absorption band from the π-conjugated system. Time-dependent (TD)-DFT[39] calculations at the B3LYP/6-31G(d)[40,41] level of theory revealed that the absorption at around 400 nm can be attributed to the HOMO–LUMO transition, $S_0 \rightarrow S_1$ (λ_{calc} = 431.7 nm, Figures 3b and 3g), having an oscillator strength (*f*) of 0.1748. The corresponding HOMO–LUMO transition ($S_0 \rightarrow S_1$) in six-membered CPP ([6]CPP) is reported to be symmetry forbidden because the HOMO and LUMO conserve symmetry (Laporte forbidden).[42–44] A strong $S_0 \rightarrow S_5$ absorption band, which mainly corresponds to the HOMO-1–LUMO (0.44) and HOMO–LUMO + 2 (0.53) transitions, was computed with *f* = 1.0250 at λ_{calc} = 327.1 nm (Figures 3c and 3g), as found at approximately 320 nm in the experimental absorption spectrum (Figure 3a).

A structured fluorescence emission was observed in the spectra obtained under a nitrogen atmosphere; this emission, at approximately 500 nm (λ_{onset} = 433 nm, λ = 475, 505 nm), has a relatively high fluorescence quantum yield of 79% (Figure 3d), and, using this, the S_1 state energy was estimated to be approximately 66 kcal mol^{-1}. In contrast, the fluorescence quantum yields of small [*n*]CPPs (*n* = 5–8) are reported to be less than 10%. Thus, the embedded azo moiety significantly changed the electronic transition and emission character of the curved π-conjugated molecule. A similar symmetry breaking strategy to turn on HOMO–LUMO absorption and emission in small CPPs was reported by Jasti.[45] The lifetime of the fluorescence at 500 nm was determined to be τ_f = 5.0 ns under N_2 at 295 K using the time-correlated-single-photon-counting (TCSPC) method (Figure S76). Interestingly, the

fluorescence quantum yield and lifetime decreased and were shortened by about 20% in air ([O_2] = 1.9 mM) to 4.2 ns and 62%, respectively (Figures 3e and S62), suggesting that the non-fluorescence process was accelerated by molecular oxygen. Recently, Suenobu and Nakagawa reported[46] similar S_1 state quenching by molecular oxygen for [9], [12], and [15]CPPs, thus generating triplet excited states of the CPP molecules. The phosphorescence of **AZ-6CPP** was not observed, even at 77 K, under a nitrogen atmosphere, which is similar behavior to that of small [*n*]CPPs (*n* = 5–7). The triplet energy was computed to be 55.6 kcal mol^{-1} at the UB3LYP/6-31G(d) level of theory. Thus, the energy difference with the S_1 state, ΔE_{ST} = ~10 kcal mol^{-1}, is smaller than the singlet oxygen energy ($^1\Delta_g$ = 22.5 kcal mol^{-1}). The generation of the T_1 state of **AZ-6CPP** was expected in the S_1 state quenching by $^3O_2$, see Figure 4d.[47]

削除: 0

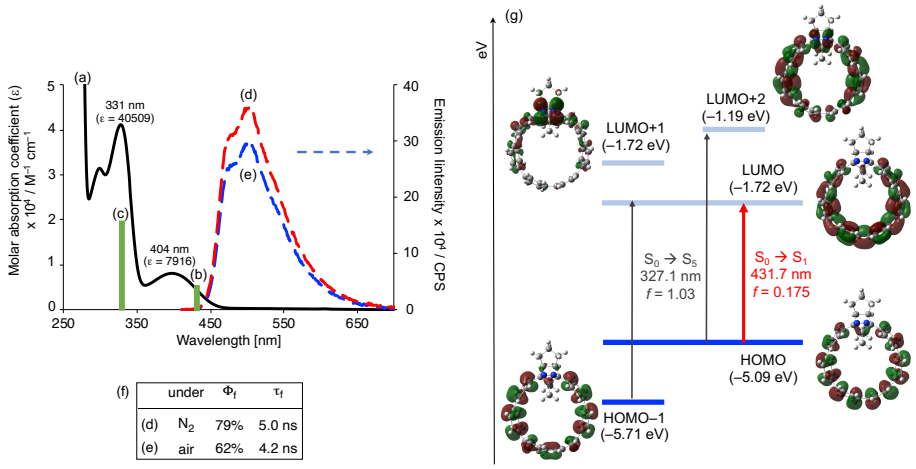

Figure 3. Absorption and emission analysis of **AZ-6CPP** in benzene. (a) UV-Vis absorption spectrum. (b) Computed $S_0 \rightarrow S_1$ transition (λ_{calc} = 431.7 nm, *f* = 0.175) at the TD-B3LYP/6-31G(d) level of

theory. (c) Computed $S_0 \rightarrow S_5$ transition (λ_{calc} = 327.1 nm, f = 1.03) at the TD-B3LYP/6-31G(d) level of theory. (d) Emission spectrum for 400-nm excitation (Abs_{400} = 0.1) under an N_2 atmosphere in benzene solution. (e) Emission spectrum for 400-nm excitation under air in benzene solution. (f) emission quantum yield (Φ_f) and lifetime (τ_f) in N_2 and air. (g) Energy diagram of Kohn–Sham orbitals and electronic transitions computed at the TD-B3LYP/6-31G(d) level of theory.

Transient absorption spectroscopy analysis of AZ-6CPP. Subnanosecond and submicrosecond transient absorption (TA) measurements of **AZ-6CPP** (Abs_{355} = 1.0) were conducted using randomly-interleaved-pulse-train (RIPT)[48] and laser flash photolysis (LFP), respectively (Figure 4). Transient species were observed with absorption peaks at approximately 540, 600, and 660 nm in the subnanosecond TA analysis just after laser irradiation in argon-saturated benzene at 298 K. These transient species did not originate from the diradical generated by photochemical denitrogenation but from the π-conjugated paraphenylene moiety because virtually no change in the UV-vis absorption spectra of the sample was observed before and after the TA measurements (Figure S56 and S57). This is reasonable because the molar extinction coefficient (ε) at 355 nm of the ππ* excitation of **AZ-6CPP** is 7000-times larger than that of the nπ* –N=N– chromophore of **AZ-2Ph**, ε = 83 $M^{-1}cm^{-1}$, whose excitation is necessary for denitrogenation to give the diradical intermediate **DR-2Ph** having a triplet ground state. The quantitative formation of the ring-closed compound **CP-2Ph** via the photochemical denitrogenation of **AZ-2Ph** has been reported with a high quantum yield of $\Phi_{N2} \approx 1.0$ (equation 1).[49]

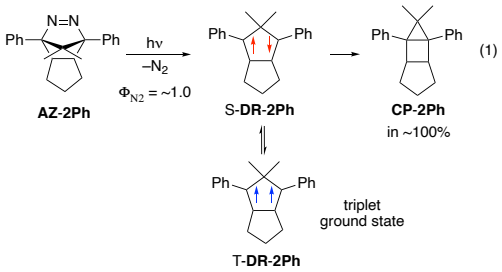

(1)

Two transient species with decay rate constants of 1.9×10^8 s^{-1} (τ = 5.2 ns, light green) and 1.5×10^5 s^{-1} (τ = 6.8 μs, light blue) were observed in the subnanosecond TA spectroscopy analysis of **AZ-6CPP** (Figures 4a and 4b). The slow decay rate constant is consistent with that obtained in the submicrosecond TA analysis (τ = 6.5 μs, Figures 4b, light blue). The absorption spectrum of short-lived species was obtained by subtracting the spectrum at 100 ns from that at 1 ns (Figure 4c, light green). The short-lived species with τ = 5.2 ns has an absorption maximum at approximately 590 nm. The transient species is assigned to singlet excited state S_1 because the lifetime of 5.2 ns is consistent with that of the fluorescence lifetime, τ_f = 5.0 ns, as shown in Figure 3f. After approximately 20 ns, another TA spectrum was obtained, and this contained absorption peaks at 540 and 660 nm (Figure 4a, light-blue) that could be assigned to the triplet state (T_1). Indeed, the lifetime of the species detected at 540 nm was significantly shortened to about 167 ns in air (Figures 4d, red line). Careful analysis of the triplet TA spectrum at 540 nm revealed that the fluorescence quenching observed in the fluorescence measurements in Figure 3e is due to the increase in the intersystem crossing (ISC) from the S_1 to the T_1 state in the presence of $^3O_2$ because the intensity of the triplet TA in air was approximately 15% higher than that obtained in Ar (Figure 4d).

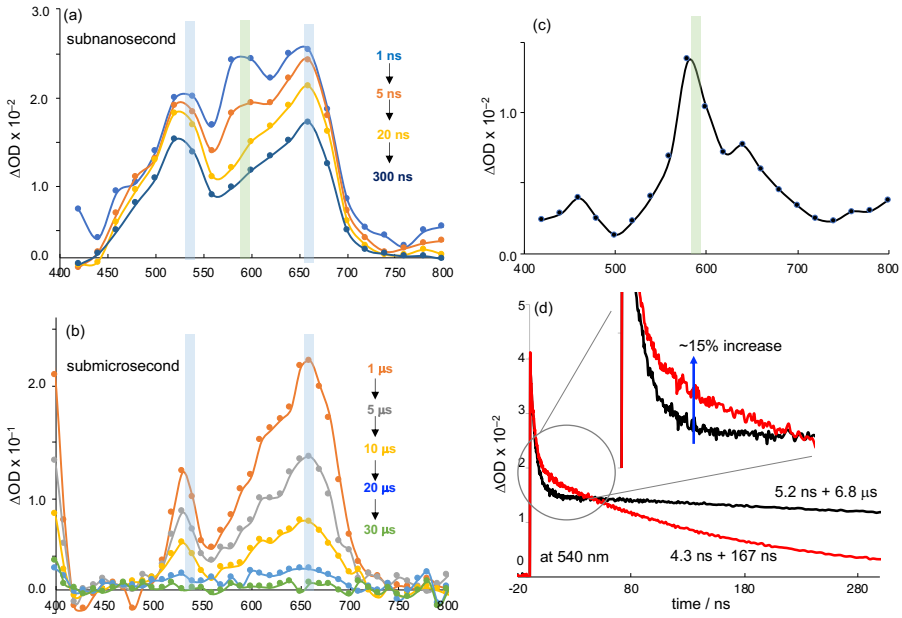

Figure 4. Time-resolved transient absorption spectra during the photolysis of **AZ-6CPP** in benzene. (a) Subnanosecond time-resolved transient absorption spectra in benzene under an Ar atmosphere (355 nm, 80 μJ/pulse, 25 ps pulse width) at 295 K. (b) Submicrosecond time-resolved transient absorption spectra in benzene under a N_2 atmosphere (355 nm, 6 mJ/pulse, 4 ns pulse width) at 295 K. (c) Transient absorption spectrum of short-lived species (singlet excited state) with τ = 5.2 ns obtained by subtracting the spectrum at 100 ns from that at 1 ns. (d) Time profile at 540 nm in the subnanosecond time-resolved spectroscopy analysis in Ar (black) and air (red).

Product analysis of the photolysis of AZ-6CPP. As found in the TA analysis, the quantum yield for the denitrogenation of **AZ-6CPP** is too low to detect diradical intermediate **DR-6CPP** directly using time-resolved spectroscopy analysis. To confirm the denitrogenation of **AZ-6CPP**, the photoreaction of **AZ-6CPP** (20 mM) using a 355-nm yttrium aluminum garnet (YAG) laser

(approximately 5.5 mJ/pulse) was monitored by ^{1}H-NMR spectroscopy at 295 K in degassed C_6D_6 solution in a sealed NMR tube under vacuum conditions (Figure 5). During the irradiation of **AZ-6CPP**, two new pairs of CH_3 groups (*a*: 0.95 and 1.82 ppm and *b*: 0.58 and 1.52 ppm in Figure 5) were observed in the photolysate with concomitant decrease of two CH_3 groups of **AZ-6CPP** (–2.36 and –0.49 ppm). After 45 h of irradiation (Figure 5d), **AZ-6CPP** was almost completely consumed under the photolysis conditions. The photoproducts were purified by column chromatography on silica gel. Both of these products were thermally labile and gradually decomposed under air conditions. Using quick column chromatography, the separated samples were sealed under N_2 and analyzed by ^{1}H-NMR, 2D-NMR, 2D-nuclear Overhauser effect (NOESY), and mass spectroscopy, demonstrating that the photoreaction products *a* and *b* are the *trans*-configured ring-closed compound t**CP-6CPP** and a methyl-group-migrated alkene product (**MG-6CPP)**, respectively (Figures S29–S47).

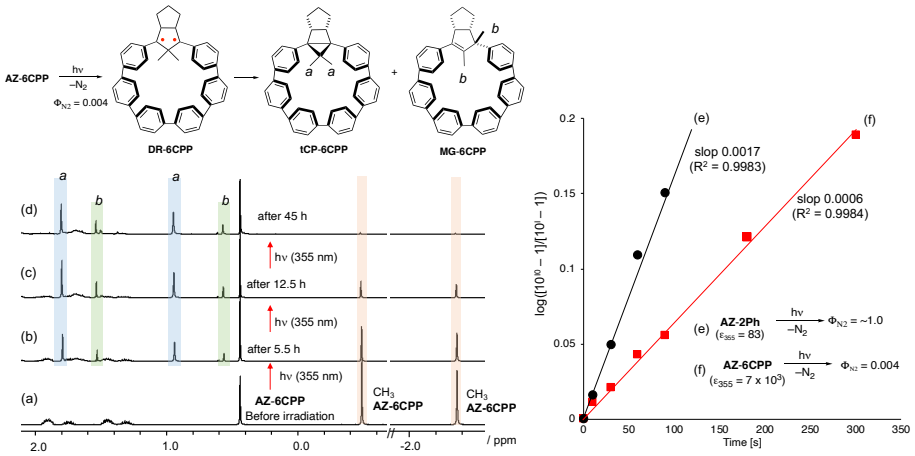

Figure 5. ^{1}H-NMR analysis (400 MHz) of the photolysis of **AZ-6CPP** (20 mM) by 355-nm laser (5.5 mJ/pulse) in degassed C_6D_6 solution. Before irradiation (a), after 2-h irradiation (b), after 12.5-h irradiation (c), and after 45-h irradiation (d). Time profile of the decomposition of azoalkanes **AZ-2Ph** (e) and **AZ-6CPP** (f) was monitored by ^{1}H-NMR spectroscopy using a 355-nm laser (5.5 mJ).

The denitrogenation quantum yield (Φ_{N2}) of **AZ-6CPP** was determined by comparing the decomposition rate with that of **AZ-2Ph**, whose denitrogenation quantum yield is known to be 1.0.[49] The decomposition of azoalkanes was monitored by ^{1}H-NMR spectroscopy (Figures 5e and 5f). The function $\log([10^{I0} - 1]/[10^{I} - 1])$, where I is the ^{1}H-NMR signal intensity of the CH_3 groups in **AZ-6CPP** and **AZ-2Ph** (Figures S27 and S28), increased linearly with irradiation time using a laser wavelength of 355-nm. The photoreaction quantum yield of **AZ-6CPP** was calculated from the ratio of the slopes of **AZ-6CPP**/**AZ-2Ph** = $\varepsilon_{AZ\text{-}6CPP}\Phi_{N2}/\varepsilon_{AZ\text{-}2Ph}\Phi_{N2}$, where $\varepsilon_{AZ\text{-}6CPP}$ (7×10^3 $M^{-1}cm^{-1}$) and $\varepsilon_{AZ\text{-}2Ph}$ (83 $M^{-1}cm^{-1}$) are the molar extinction coefficients of **AZ-6CPP** and **AZ-2Ph** at 355 nm. From the analysis, the denitrogenation quantum yield of **AZ-6CPP** was determined to be 0.004 (0.4%). The

low quantum yield is a result of the 355-nm light being mainly absorbed by the curved π-conjugated moiety, as suggested by the TA analysis (Figure 4).

EPR measurements. Although the quantum yield of the photochemical denitrogenation **AZ-6CPP** is very low, it might be possible to observe **DR-6CPP** directly during the photolysis of **AZ-6CPP** using electron paramagnetic resonance (EPR) spectroscopy analysis because of its high sensitivity to paramagnetic species. Thus, low-temperature photolysis of **AZ-6CPP** (11 mM) in degassed 2-methyltetrahydrofuran (2MTHF) was conducted using a Hg lamp (λ_{emi} > 250 nm) at 4 K (Figure 6). After 4 h, a typical signal stemming from persistent triplet species was observed at 1650 gauss (G), and this was assigned to the $\Delta M_S = \pm 2$ forbidden transition. In addition to the half-field signal at 1650 G, the allowed transitions of $\Delta M_S = \pm 1$ (2977 (z_1), 3142 (xy_1), 3560 (xy_2), and 3731 G (z_2)) were observed at a resonance frequency of 9.40 GHz. From the z-signals, the zero-field splitting (zfs) parameters were determined to be $|D/hc| = 0.035$ cm^{-1} and $|E/hc| = < 0.001$ cm^{-1} (Figure 6a).[13] The triplet EPR spectrum was consistent with the simulated spectrum by inputting zfs parameters of $|D/hc| = 0.035$ cm^{-1} and $|E/hc| = 0$ cm^{-1} (Figure 6b), and the average distance between the two dipoles was determined to be 4.20 Å using the point dipole approximation,[50] which is longer than 3.76 Å in **DR-2Ph** ($|D/hc| = 0.050$ cm^{-1} and $|E/hc| = < 0.001$ cm^{-1})[51,52] generated from **AZ-2Ph** (equation 1), indicating that the diradical is more delocalized over the benzene rings.[51]

To obtain more information about the triplet diradical generated in the photolysis of **AZ-6CPP**,

the spin densities of diradicals T-**DR-2Ph** and T-**DR-6CPP** were computed at the UB3LYP/6-31G(d) level of theory. The spin density at the benzylic carbon of T-**DR-2Ph** was computed to be 0.753. The corresponding value for T-**DR**$_{exo}$-**6CPP** was calculated to be 0.706. A smaller value of 0.665 was found for the endo isomer, T-**DR**$_{endo}$-**6CPP**. To confirm the structural assignment of the triplet diradical having a smaller *D* value ($|D/hc|$ = 0.035 cm^{-1}) than that of **DR-2Ph** ($|D/hc|$ = 0.050 cm^{-1}), the zfs parameters *D* and *E* were computed at the (RO)BP/EPR-II//UB3LYP/6-31G(d)[53,54] level of theory using ORCA 4.2.1[55,56] (Figure 6c). The zfs parameters of the parent triplet diradical T-**DR-2H** ($|D/hc|$ = 0.084 cm^{-1} and $|E/hc|$ = 0.002 cm^{-1})[57,58] were also calculated at the same level of theory to confirm the reliability of the computation. As shown in Figure 6c, the experimentally obtained $|D/hc|$ values in wavenumbers, 0.084 and 0.050 cm^{-1} for T-**DR-2H** and T-**DR-2Ph**, respectively, were well reproduced by the computations, i.e., 0.088 and 0.050 cm^{-1}, respectively. The *D* values for T-**DR**$_{exo}$-**6CPP** and T-**DR**$_{endo}$-**6CPP** were computed to be 0.041 and 0.034 cm^{-1}, respectively. Thus, the triplet signals observed in the photolysis of **AZ-6CPP** (Figure 6a) were assigned to T-**DR**$_{endo}$-**6CPP**. Although T-**DR**$_{endo}$-**6CPP** was calculated to be less stable than T-**DR**$_{exo}$-**6CPP** by 7.9 kcal mol^{-1}, the assignment is reasonable because **AZ-6CPP** (Scheme 1) has the same configuration as endo isomer **DR**$_{endo}$-**6CPP**, featuring a *trans*-configuration of the dimethylmethano moiety with cyclopentane ring.

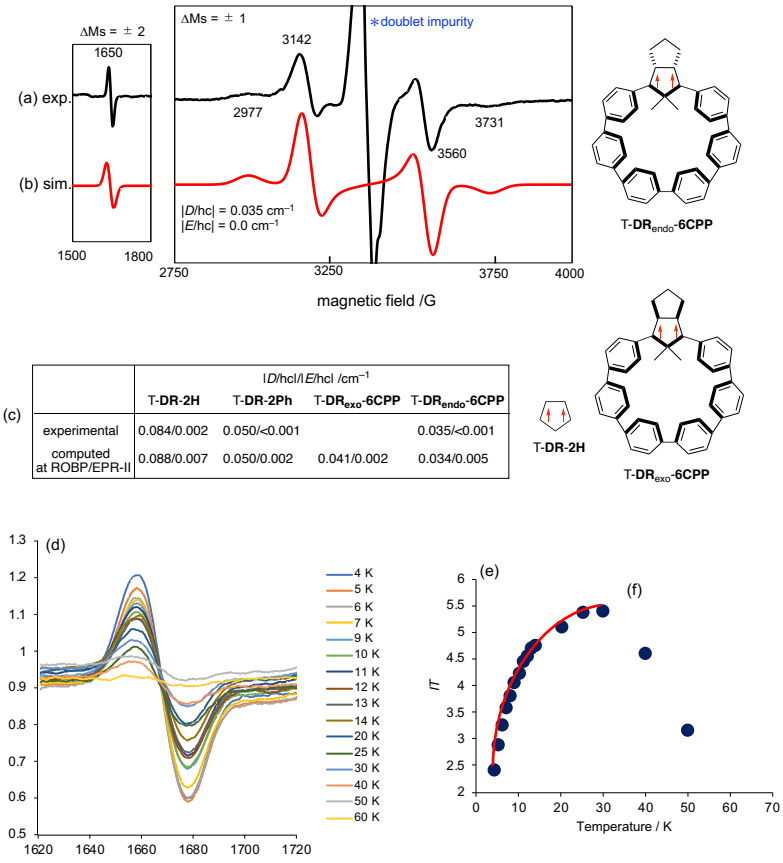

Figure 6. EPR spectrum of the photolysis of **AZ-6CPP** (11 mM) using an Hg lamp (> 250 nm) in 2MTHF matrix in a sealed quartz-tube at 4 K under vacuum conditions (resonance frequency = 9.40 GHz) (a). EPR spectrum simulated using the zfs parameters $|D/hc| = 0.035$ cm^{-1} and $|E/hc| = 0.00$ cm^{-1} (b). Experimental and computed zfs parameters (D and E) for diradicals T-**DR-2H**, T-**DR-2Ph**, and T-**DR-6CPP** (c). Temperature dependency of the intensity of the EPR signal at 1650 G (d). IT-T plot (e). Least squares fit for Bleaney–Bowers analysis (f).

The temperature dependency of the intensity of the triplet signal at 1650 G was examined to determine the ground state spin multiplicity. The intensity measurements were conducted at a

microwave power of 20 mW, for which signal saturation was not observed, even at 4 K (Figure S82). After the generation of **DR-6CPP** at 4 K, the temperature was increased by 1 K to 15 K, then by 5 K until 30 K (Figure 6d). Surprisingly, the triplet signal suddenly weakened at 40 K (Figure 6d) and the signal intensity did not return to the original intensity at 4 K. After re-generation of **DR-6CPP** at 6 K, the sample was heated up to 30 K then re-cooled to 6K to confirm the thermal stability of **DR-6CPP** at 30 K. The intensity of 0.545 at 6 K before warming the sample was nearly the same to 0.547 at 6K after re-cooling the sample to 6K (Figure S83), suggesting that **DR-6CCP** is persistent below 30 K. The high reactivity, even at 40 K, is significantly different from the persistent character of T-**DR-2Ph** at 77 K.[59] In the *IT*-*T* plot below 30 K (Figure 6d), the *IT* value gradually decreased with decreasing temperature, indicating that the triplet state is thermally populated as an excited state. From the least-squares fit for Bleaney–Bowers analysis (R^2 = 0.9825, number of points = 14, Figures 6e,f),[60] the singlet(E_S)–triplet(E_T) energy gap ($\Delta E_{ST} = 2J/k_B = E_S - E_T$, J/k_B: exchange interaction) was determined to be –15.8 ± 0.5 cal mol^{-1} (= –7.9 K, J/k_B = 3.95 K), demonstrating the singlet ground state of **DR**$_{endo}$-**6CPP** (Figure 6e). Thus, the ground state spin multiplicity was switched by the curved macrocyclic structure. The maximum in the *I*-*T* plot (Figure S84) was not clearly observed in the temperature range of 4-30 K because the exchange interaction value was J/k_B = 3.95 K.

削除: ,
書式を変更: フォント : 太字
書式を変更: フォント : 太字
削除: #
削除: only
削除:
書式を変更: 下付き
削除:
書式を変更: フォント : 斜体
書式を変更: フォント : 斜体
書式を変更: 下付き
書式を変更: フォント : 斜体
書式を変更: 下付き
削除: 66
削除: 2
削除: J
削除: from
書式を変更: フォント : 太字
書式を変更: 下付き
書式を変更: フォント : 太字
削除: found to be
書式を変更: 蛍光ペン（なし）
削除: #

Discussion

As found in the EPR experiments, the ground-state spin multiplicity switched from triplet in **DR-2Ph**

to singlet in **DR$_{endo}$-6CPP**, which has a curved π-conjugated structure, although the singlet–triplet energy spacing is small. To gain more insight into the macrocyclic effect, the singlet–triplet energy spacings of **DR-2Ph**, **DR$_{endo}$-6CPP**, and **DR$_{endo}$-2Ph'** were computed using DFT (CAM-B3LYP/6-31G(d))[61] and complete active space self-consistent field (CASSCF)[62] calculations in Gaussian 16[63]. The structure of **DR$_{endo}$-2Ph'** was obtained by replacing the middle four benzene rings with two hydrogen atoms in **DR$_{endo}$-6CPP** without optimizing the curved structure of the two benzene rings at the radical sites (Figure 7c). The open-shell singlet state was computed using the broken-symmetry (BS)[64] approach for the DFT calculations. The energy corrections were conducted using the complete active space second-order perturbation theory (CASPT2)[65] for the CASSCF calculations. Thus, the effect of the curvature on the open-shell singlet–triplet energy spacing was appropriately computed.

書式を変更: 下付き

書式を変更: 下付き

書式を変更: 下付き

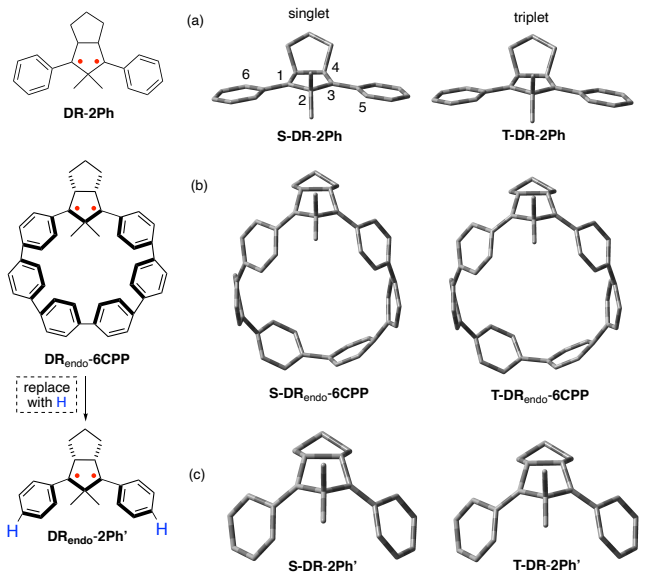

		dihedral angle /° (C1-C2-C3-C4)	bent angle /° (C5-C2-C6)	bond length /pm (C1-C3)
DR-2Ph	singlet	6.5	167	240.4
	triplet	6.6	157	240.2
DR$_{endo}$-6CPP (DR$_{endo}$-2Ph')	singlet	47.4	115	229.7
	triplet	42.7	120	236.6

computed at the (U)CAM-B3LYP/6-31G(d) level of theory

Figure 7. Structures of **DR-2Ph** (a), **DR$_{endo}$-6CPP** (b), and **DR$_{endo}$-2Ph'** (c) optimized at the UCAM-B3LYP/6-31G(d) level of theory. Hydrogen atoms are omitted for clarity.

First, the molecular structures **DR-2Ph** and **DR$_{endo}$-6CPP** were optimized at the BS UCAM-B3LYP/6-31G(d) level of theory. Nearly planar structures were found in the cyclopentane-1,3-diyl moiety for **DR-2Ph** (Figure 7a), and the C1-C2-C3-C4 dihedral angles were computed to be approximately 6.5° for both triplet and singlet states. The two planar benzene rings have a coplanar orientation with the cyclopentane-1,3-diyl moiety, as shown by the C5-C2-C6 angles, which were

削除:

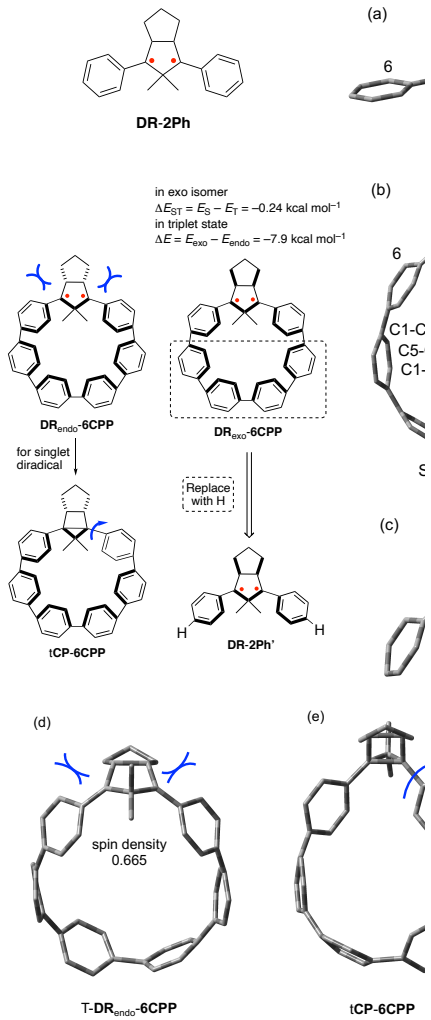

削除: , T-**DR$_{endo}$-6CPP** (d), and t**CP-6CPP** (e)

書式を変更: 下付き

削除:

書式を変更: 下付き

削除: 4.0

calculated to be 167 and 157° for the singlet and triplet states. The distances between C1 and C3 were found to be 240.4 and 240.2 pm in the singlet and triplet states, respectively. Thus, nearly the same molecular structures were found in the singlet and triplet states of **DR-2Ph**.

In contrast to the planar and flat structures of **DR-2Ph**, puckered and bent structures were found in **DR$_{endo}$-6CPP** at the same level of theory (Figures 7b). Puckered structures having C1-C2-C3-C4 dihedral angles of 47.4° and 42.7° were obtained for the singlet and triplet **DR$_{endo}$-6CPP**, respectively (Figure 7b). The C5-C2-C6 angles (bending of the benzene rings) in the singlet and triplet states **DR$_{endo}$-6CPP** were computed to be 115° and 120°, respectively, which are smaller than that of **DR-2Ph** (~160°). In particular, the atomic distance of 229.7 pm in **S-DR$_{endo}$-6CPP** was significantly shorter than that in the triplet state **T-DR$_{endo}$-6CPP**, 236.6 pm, and in the singlet and triplet states in **DR-2Ph** (240.4 and 240.2 pm).

To understand the electronic structure of **DR-2Ph** and **DR$_{endo}$-6CPP**, the HOMO and LUMO occupation numbers in their singlet states were compared (Figure 8). The occupation numbers of **S-DR-2Ph** and **S-DR$_{endo}$-6CPP** were determined at the CASSCF(2,2)/6-31G(d) level of theory. As clearly shown in the HOMO and LUMO images (Figure 8a), parallel alignment of the p-orbitals was found in **S-DR-2Ph**. The occupation numbers of electrons in the HOMO (ψ_A) and LUMO (ψ_S) orbitals in **S-DR-2Ph** were computed to be 1.04 and 0.96, respectively, indicating a negligible bonding interaction between the two radicals, that is, nearly pure singlet diradical character in **S-DR-2Ph**. Thus,

削除： 171…67 and 157° for both …he singlet and triplet and singlet …tates. The distances between C1 and C3 were found to be 240.9 … and 240.8 … [1]

書式を変更： 下付き

削除： Three isomers, S-**DR$_{exo}$-6CPP**, T-**DR$_{exo}$-6CPP**, and T-**DR$_{endo}$-6CPP**, were optimized as equilibrium structures (Figures 7b,d). The remaining possible isomer, the endo-configured singlet diradical S-**DR$_{endo}$-6CPP**, could not be obtained and instead optimized to the ring-closed compound t**CP-6CPP** (Figure 7e). As clearly suggested by the optimized structure of T-**DR$_{endo}$-6CPP** (Figure 7d), the steric repulsion of the phenyl rings with the cyclopentane ring is key to the energetic destabilization of S-**DR$_{endo}$-6CPP** to form t**CP-6CPP** on optimization. The phenyl ring in t**CP-6CPP** can twist to avoid steric repulsion (Figure 7e) because the phenyl ring does not need to stabilize the radicals in **DR$_{endo}$-6CPP**. As mentioned above, the endo isomer in T-**DR$_{endo}$-6CPP** was less stable than the exo isomer T-**DR$_{exo}$-6CPP** by 7.9 kcal mol^{-1}. …uckered structures having C1-C2-C3-C4 dihedral angles of 42…7.4° and 42.724… were obtained for the exo isomers of …inglet and triplet **DR$_{exo}$…R$_{endo}$-6CPP**, respectively (Figure 7b). The C5-C2-C6 angles (bending of the benzene rings) in S-**DR$_{exo}$-6CPP** the singlet and triplet states **DR$_{endo}$-6CPP** was …ere computed to be 1153… and 120°, respectively, which is …re much …maller than that of T-**DR$_{exo}$-6CPP** (135°) and …hat of **DR-2Ph** (171…160°). In particular, the atomic distance of 231.6 …29.7 pm in S-**DR$_{exo}$-6CPP**…-**DR$_{endo}$-6CPP** wasis…significantly shorter than that …hat in the triplet state T-**DR$_{exo}$-6CPP**…-**DR$_{endo}$-6CPP**, 239.8…36.6 pm, and … [2]

書式を変更： 下付き

削除： and S-**DR$_{exo}$-6CPP**

書式を変更： フォント：太字（なし）

削除： /BS-UB3LYP/…-31G(d) level of theory. As clearly shown in the HOMO and LUMO images (Figure 8a), parallel alignment of the p-orbitals was found in S-**DR-2Ph**. The occupation numbers of electrons in the HOMO (ψΨ…) and LUMO (ψΨ … [3]

the triplet ground state is reasonable for **DR-2Ph**. In contrast, a bent conformation was found in S-**DR**$_{endo}$**-6CPP**, which suggests a bent-type (banana-like) bonding interaction between the two radical sites (Figure 8b). Indeed, S-**DR**$_{endo}$**-6CPP** possesses a bonding combination of HOMO (ψ_S) and antibonding LUMO (ψ_A), whose orbital order is, interestingly, opposite in S-**DR-2Ph** (Figure 8a). The switch in the HOMO–LUMO conversion in **DR-2Ph** is a result of through-bond interactions.[12,25,66–70] The occupation numbers in the bonding (ψ_S) and anti-bonding (ψ_A) orbitals were found to be 1.47 and 0.53, respectively, and the bond order between the radical sites were calculated to be 0.47 from the occupation numbers in the bonding and anti-bonding orbitals.

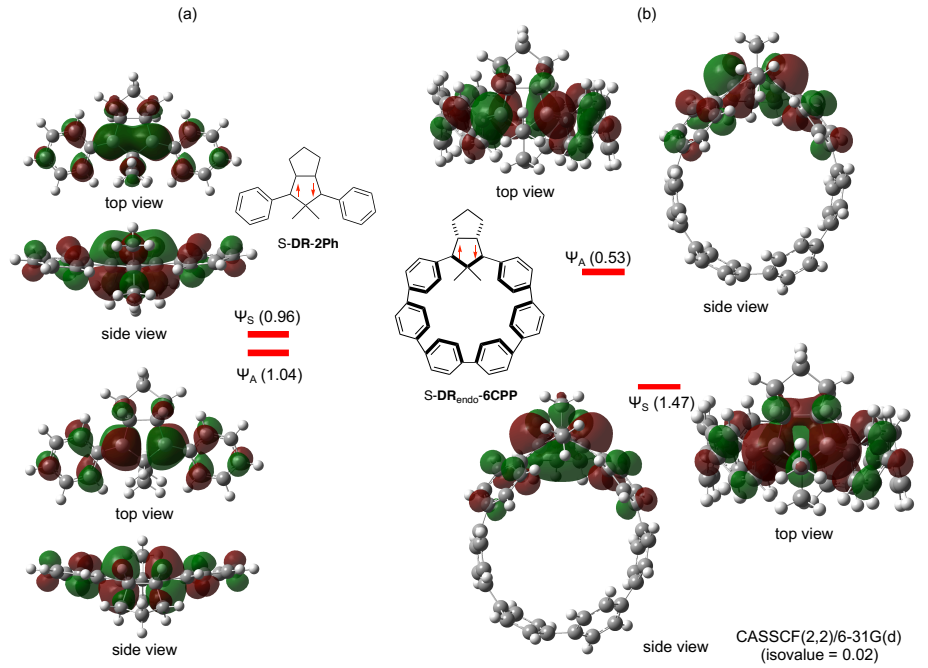

書式を変更：下付き
削除：exo
削除：exo
削除：Ψ
書式を変更：下付き
削除：Ψ
削除：49
削除：51
削除：,
削除：was
削除：49

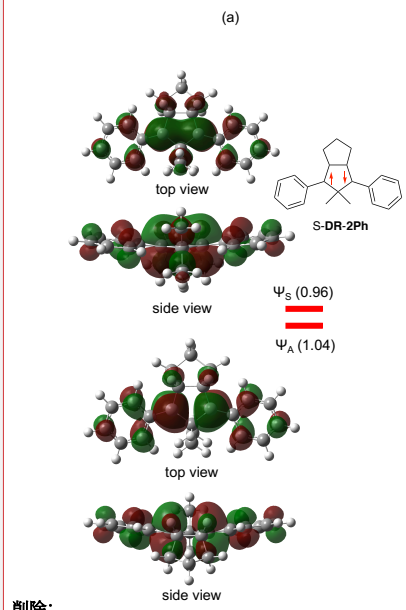

削除：

Figure 8. HOMO and LUMO orbitals and their occupation numbers in S-**DR-2Ph** (a) and S-**DR**$_{endo}$-**6CPP** (b) calculated at the CASSCF(2,2)/6-31G(d) level of theory.

The singlet–triplet energy spacing in **DR-2Ph** and **DR**$_{endo}$**-6CPP** was computed at the UCAM-B3LYP/6-31G(d) level of theory (Table 1). In contrast to the triplet ground state of diradicals **DR-2Ph**, $\Delta E_{ST} = E_S - E_T = +0.20$ kcal mol^{-1}, the singlet was calculated to be the ground state, having energy preference by 1.77 kcal mol^{-1}, in **DR**$_{endo}$**-6CPP** (entries 1 and 2). To confirm the energy gap obtained in the DFT calculations, the **DR-2Ph'** diradical having curved benzene rings was used for the computation of the energy gap at the CASPT2(14,14)/cc-pVDZ level of theory using OpenMolcas[71] because the π-electrons in **DR-6CPP** are too large to compute the energy gap using the CASPT2 method (Table S7 and Figure S134). Singlet ground state with $\Delta E_{ST} = E_S - E_T = -3.84$ and -6.35 kcal mol^{-1} was found for **DR**$_{endo}$**-2Ph'** at the CASSCF(14,14)/cc-pVDZ and CASPT2(14,14)/cc-pVDZ level of theory, respectively (entry 3). At the same level of theory, the triplet ground state was confirmed, having $\Delta E_{ST} = +0.20$ kcal mol^{-1}, for **DR-2Ph** (entry 1). Thus, the singlet preference of **DR**$_{endo}$**-6CPP** (Figure 6e) is rationalized to result from the puckered structure of the diradical. The bent-bonding interaction between the two radical sites is the key reason for the singlet ground state in S-**DR**$_{endo}$**-6CPP** (Figure 8b).

Table 1. Singlet–triplet energy gap ($\Delta E_{ST} = E_S - E_T$) in **DR-2Ph**, **DR**$_{endo}$**-6CPP**, and **DR-2Ph'**.

Entry	Diradical	Singlet–triplet energy gap/kcal mol^{-1} ($\Delta E_{ST} = E_S - E_T$)

削除： and S-**DR**$_{exo}$**-6CPP** (b)

削除：

削除：/BS-UB3LYP/

書式を変更：下付き

削除：exo

削除：14

書式を変更：蛍光ペン（なし）

削除：a small

削除：0.24

削除：xo

削除：/

削除：exo

削除：A s

削除：2.05

削除：**DR-2Ph'**

書式を変更：フォント：太字

書式を変更：フォント：太字，下付き

書式を変更：フォント：太字

削除：ry 3

削除：, as exemplified by the singlet ground state of **DR**$_{exo}$**-6CPP** and **DR-2Ph'**

削除：Thus, t

書式を変更：下付き

削除：**DR**$_{exo}$

		UB3LYP/6-31G(d)	CASSCF(14,14)/ cc-pVDZ	CASPT2(14,14)/ cc-pVDZ
1	**DR-2Ph**	+0.20	+0.37	+0.20
2	**DR$_{endo}$-6CPP**	−1.77	n.d.	n.d.
3	**DR-2Ph'**	−1.20	−3.84	−6.35

To obtain more insights into the macrocyclic effect on the reactivity of the diradicals, the ring-closing reaction to yield **CP-6CPP** was computed, thus allowing comparison with the corresponding reaction for **DR-2Ph** (Figure 9). First, the ring-closing reaction of S-**DR-2Ph** to **CP-2Ph** was computed at the BS-(U)CAM-B3LYP/6-31G(d) level of theory. The kinetically favored ring-closing reaction was found to give a *cis*-configured compound, **cCP-2Ph**, with an energy barrier of 13.6 kcal mol^{-1} (Figure 9a). A slightly high energy barrier, 13.7 kcal mol^{-1}, was calculated for the reaction to the *trans*-configured compound, **tCP-2Ph**. The repulsive interaction between Ph and CH_2 groups in the transition state **TSt** increases the energy of **TS**t for the formation **tCP-2Ph**, whose observation is similar for the previously reported kinetically favored formation of *cis*-isomer.[72] The persistent character of **DR-2Ph** at low temperature (< 100 K) is reasonable on the basis of the relatively large energy barriers for the radical-radical coupling reaction obtained by computation.

A small energy barrier, 1.87 kcal mol^{-1}, was calculated for the ring-closing reactions in the exo-isomer of S-**DR-6CPP**, S-**DR$_{exo}$-6CPP** (black line, Figure 9b). In the reaction of endo-isomer S-**DR$_{endo}$-6CPP**, a clear energy barrier was not found during the scan calculation in the C1–C3 bond-formation process to give the ring-closed compound **tCP-6CPP** (Figure S88); thus, the energy barrier from S-**DR$_{endo}$-6CPP** to **tCP-6CPP** is should be very small (blue line, Figure 9b). The observed high

削除: 14
削除: 0.24
削除: xo
削除: 52
削除: 0.75
削除: 2.05
削除: 11
削除: 4
削除: 12
削除: .3
書式を変更: フォント : 太字
書式を変更: フォント : 太字
削除: Interestingly, a small energy barrier, 0.4 kcal mol^{-1}, was calculated for the ring-closing reactions in S-**DR$_{exo}$-6CPP** (Figure 9b).
削除: As mentioned above, the endo-isomer S-**DR$_{endo}$-6CPP** was not found to be an equilibrium structure, and structure optimization yielded the
削除: #
削除: (Figure 5)
書式を変更: 蛍光ペン（なし）
削除: negligible

reactivity of **DR$_{endo}$-6CPP**, even at 40 K, under low-temperature matrix conditions is reasonable because of the very small energy barrier. In the photolysis of **AZ-6CPP**, another product, **MG-6CPP**, was formed (Figure 6). A relatively large energy barrier of 41.9 kcal mol^{-1} was computed for the methyl migration reaction in S-**DR$_{endo}$-6CPP** (red line, Figure 9b), which is much higher in energy than that of the ring-closing reaction. The large energy barrier computed for the migration reaction suggests that the formation of **MG-6CPP** stems from an electronically excited state. Photolysis of the matrix isolated **DR-2Ph** has been reported to produce the corresponding methyl migration product, **MG-2Ph**.[59] The photolysis of t**CP-2Ph** using 266 nm irradiation, indeed, produced **MG-2Ph** (Figures S85-87). Thus, compound **MG-6CPP** is proposed to be formed in the secondary photoreaction of **CP-6CPP**.

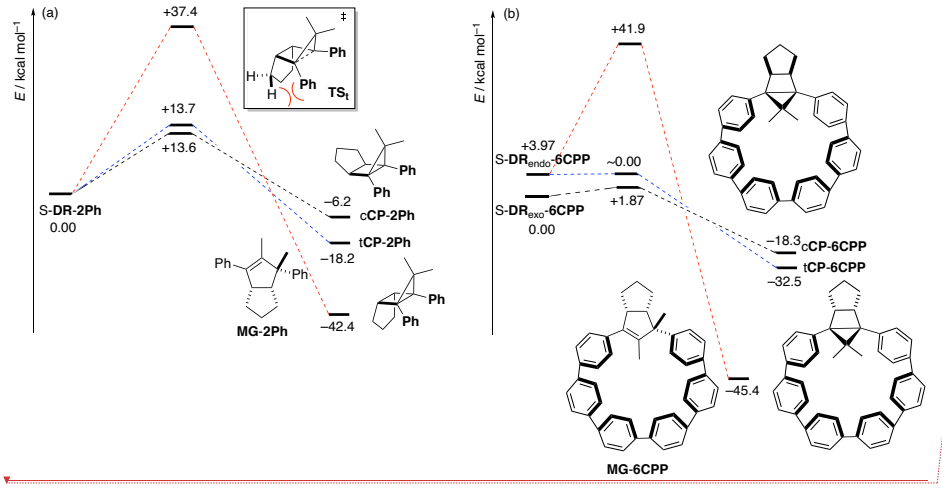

Figure 9. Computations on thermal reactivity of singlet diradicals S-**DR-2Ph** and S-**DR-6CPP** at the (U)CAM-B3LYP/6-31G(d) level of theory.

書式を変更: 下付き
削除: negligible
削除: s
削除: 37.
削除: 6
書式を変更: フォント : 太字
書式を変更: フォント : 太字, 下付き
書式を変更: フォント : 太字
削除: 3
削除: 5
削除:

We wondered "why are the energy barriers from S-**DR**$_{endo}$-**6CPP** to t**CP-6CPP** and S-**DR**$_{exo}$-**6CPP** to c**CP-6CPP** so small?" As shown in Figure 8b, the puckered structure of S-**DR**$_{endo}$-**6CPP**, which already possesses bent-bonding character, is one of the reasons for the small energy barrier. The similar molecular structures were found in S-**DR**$_{exo}$-**6CPP** (Figure S136). To gain more insight into the high reactivity of **DR-6CPP**, the molecular strain energies were computed for **AZ-6CPP**, S-**DR**$_{endo}$-**6CPP**, T-**DR**$_{endo}$-**6CPP**, S-**DR**$_{exo}$-**6CPP**, T-**DR**$_{exo}$-**6CPP**, t**CP-6CPP**, and c**CP-6CPP** using equation 2 in Table 2. The strain energies of **AZ-6CPP** and **DR-6CPP** were determined to be 79-85 kcal mol^{-1} (entries 1–5), similar to that of [7]CPP (84 kcal mol^{-1})[73] calculated at the B3LYP/6-31G(d) level of theory. The strain energy of **DR**$_{endo}$-**6CPP** was higher by ~5 kcal mol^{-1} than the exo isomer (entries 2-5). Surprisingly, the strain energies of the ring-closed **CP-6CPP** were found to be approximately 10 and 15 kcal mol^{-1} lower than those of the diradical intermediates S-**DR**$_{exo}$-**6CPP** and S-**DR**$_{endo}$-**6CPP**, respectively (entries 6,7), although the ring size of **CP-6CPP** is, in principle, smaller than that of **DR-6CPP** by one carbon. The computational results demonstrate that the ring-closing reaction releases molecular strain, suggesting that the small energy barriers in the ring-closing process in **DR-6CPP** were accelerated by the release of molecular strain, as well as the bonding interaction in S-**DR-6CPP**. A question quickly arises: "Why is the molecular strain in **CP-6CPP** smaller than that in **DR-6CPP** in spite of the smaller ring size in **CP-6CPP** than that in **DR-6CPP**." Careful analysis of the optimized structures revealed that there is greater steric repulsion between the methyl group and the adjacent benzene ring in S-**DR-6CPP** than that in c**CP-6CPP** because the phenyl ring can twist in

書式を変更: フォント : 太字（なし）, 下付き

削除: **DR**$_{exo}$

書式を変更: フォント : 太字

書式を変更: フォント : 太字, 下付き

書式を変更: フォント : 太字

書式を変更: 蛍光ペン（なし）

削除: #

削除: **DR**$_{exo}$

削除: **DR**$_{exo}$

削除: c**CP-6CPP**, and

書式を変更: フォント : 太字

書式を変更: フォント : 太字

削除: approximately

削除: 75

削除: 3

削除: 8

削除: 72

削除: same

書式を変更: フォント : 太字

書式を変更: 下付き

書式を変更: フォント : 太字

書式を変更: 上付き

削除: 10

書式を変更: フォント : 太字

書式を変更: フォント : 太字

書式を変更: フォント : 太字

書式を変更: フォント : 太字

削除: ies

削除: and

削除: 4 and 5

CP-6CPP (see the optimized structures in Table 2).

Table 2. Molecular strain energy of **AZ-6CPP**, S-**DR**$_{endo}$**-6CPP**, T-**DR**$_{endo}$**-6CPP**, **tCP-6CPP**, **cCP-6CPP** at (U)CAM-B3LYP/6-31G(d) level of theory.

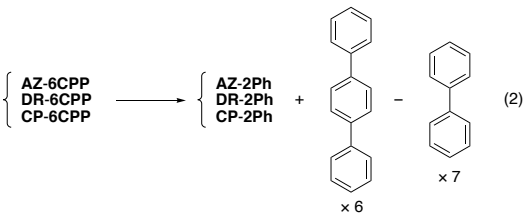

entry	molecule	strain energy/kcal mol^{-1}
1	**AZ-6CPP**	78.8
2	S-**DR**$_{endo}$**-6CPP**	82.6
3	T-**DR**$_{endo}$**-6CPP**	84.6
4	S-**DR**$_{exo}$**-6CPP**	78.7
5	T-**DR**$_{exo}$**-6CPP**	78.7
6	**tCP-6CPP**	68.3
7	**cCP-6CPP**	66.5

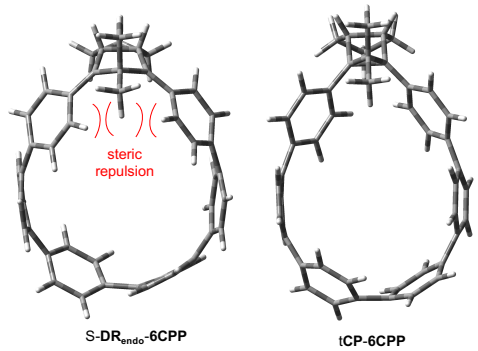

As shown by pioneering studies on the effects of size on the electronic character of CPPs,[33,35]

削除: xo
削除: xo
削除: cCP-6CPP, and
書式を変更: フォント : 太字
書式を変更: フォント : 太字
削除:
削除: 6.1
削除: DRexo
削除: 74.1
削除: DRexo
削除: 74.5
削除: 4
... [4]
書式付きの表
削除: 5
削除: 65.7
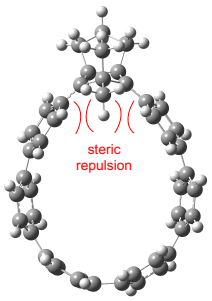

削除:

the size-dependent change in molecular structure and ground state spin-multiplicity is particularly interesting in diradicals embedded in cycloparaphenylenes: **DR**$_{endo}$-(n + 3)**CPP**s (n = 0–5). Thus, the reaction energy ($\Delta_r E$ in kcal mol^{-1}) was computed for the formation of **t**CP-(n + 3)**CPP** from S-**DR**$_{endo}$-(n + 3)**CPP**s (Table 3). Interestingly, ring-closed **t**CP-**3CPP** was not found to be an equilibrium structure at the restricted B3LYP/6-31G(d) level of theory, and optimization yielded the ring-opened diradical S-**DR**$_{endo}$-**3CPP** featuring the quinoidal form (entry 1). Thus, the intramolecular cyclization of S-**DR**$_{endo}$-**3CPP** to **t**CP-**3CPP** is energetically disfavored, although the strain energy (*SE*) of S-**DR**$_{endo}$-**3CPP** was computed to be high, SE_{DR} = 91.3 kcal mol^{-1}. The exothermicity ($\Delta_r E$) of the intramolecular cyclization is prone to increase with increasing size (n) of the paraphenylene moiety (entries 2–6). The strain energies (SE_{CP} and SE_{DR}) in **t**CP-(n+3)**CPP** and S-**DR**$_{endo}$-(n+3)**CPP** were found to decrease with increasing macrocyclic ring size (entries 2-6). The strain energy (SE_{DR}) in S-**DR**$_{endo}$-**3CPP** was smaller than S-**DR**$_{endo}$-**4CPP** (entries 1,2). The quinoidal form of S-**DR**$_{endo}$-**3CPP** would be the reason for it.

The effect of the ring size on the singlet–triplet energy gap ($\Delta E_{ST} = E_S - E_T$) computed at the (U)CAM-B3LYP/6-31G(d) level of theory was also analyzed in **DR**$_{endo}$-(n+3)**CPP**, and the results are summarized in Table 3. Interestingly, the energy gap was found to be significantly dependent on the ring size. In particular, as the size of the rings increases, there is a tendency for the triplet state to become more stable. For example, a significant preference (by 21.3 kcal mol^{-1}) for the singlet state was found for **DR-3CPP** (n = 0, entry 1), whereas the triplet ground state was computed for **DR**$_{endo}$-

削除：xo

削除：cCP

削除：xo

削除：cCP

削除：DR$_{exo}$

削除：DR$_{exo}$

削除：cCP

削除：DR$_{exo}$

削除：c

削除：DR$_{exo}$

削除：DR$_{exo}$

削除：DR$_{exo}$

削除：DR$_{exo}$

削除：15

7CPP (n = 4, entry 5) and **DR$_{endo}$-8CPP** (n = 5, entry 6). It should be noted that the singlet–triplet energy gap drastically increased to 4.5 and 21.3 kcal mol^{-1} (i.e., singlet preference) for **DR$_{endo}$-4CPP** and **DR$_{endo}$-3CPP**, respectively (entries 1 and 2). The singlet states of **DR$_{endo}$-3CPP** and **DR$_{endo}$-4CPP** are not perfect open-shell molecules; rather, they are nearly closed-shell molecules (quinoidal structures) because the HOMOs of S-**DR$_{endo}$-3CPP** and S-**DR$_{endo}$-4CPP** were computed to be 1.91 and 1.64 at the CASSCF(2,2)//BS-UCAM-B3LYP/6-31G(d) level of theory (entries 1 and 2), demonstrating that the quinoidal structures S-**DR$_{endo}$-3CPP** and S-**DR$_{endo}$-4CPP** are important. As the size of the rings increases, there is a trend for the singlet state to increase in diradical character, as judged by the occupation numbers of the HOMOs and LUMOs. Finally, a triplet ground state was found for **DR$_{endo}$-7CPP** and **DR$_{endo}$-8CPP** due to the small difference of the occupation numbers in HOMO (1.16 and 1.12) and LUMO (0.84 and 0.88) (Figure 8), having ΔE_{ST} = +0.13 and +0.19 kcal mol^{-1} (entries 5 and 6). Similar to **DR-2Ph** (Figure 7), nearly the planar structure having C1-C2-C3-C4 dihedral angles of 22 and 15° and the normal atom distance of C1–C3 (240.4 and 241.1 pm) were found in S-**DR$_{endo}$-7CPP** and S-**DR$_{endo}$-8CPP**, respectively.

書式を変更：下付き

削除：6.58

削除：15

削除：**DR$_{exo}$**

削除：$_{exo}$

削除：the spin expectation values <S^2> were calculated to be 0.00 and 0.30, respectively, using the BS-DFT method

削除：$_{exo}$

削除：$_{exo}$

削除：Indeed, the occupation numbers of the HOMOs of S-**DR$_{exo}$-3CPP** and S-**DR$_{exo}$-4CPP** were computed to be 1.91 and 1.75, respectively, at the CASSCF(2,2)//BS-UB3LYP/6-31G(d) level of theory (entries 1 and 2).

書式を変更：フォント：太字（なし）

書式を変更：下付き

削除：13

削除：87

削除：08

削除：y

削除：16

削除：240.6

削除：

削除：$_{xo}$

Table 3. Effect of the ring size on the singlet–triplet energy gap ($\Delta E_{ST} = E_S - E_T$) in **DR$_{endo}$-[*n* + 3]CPP** (*n* = 0–5).

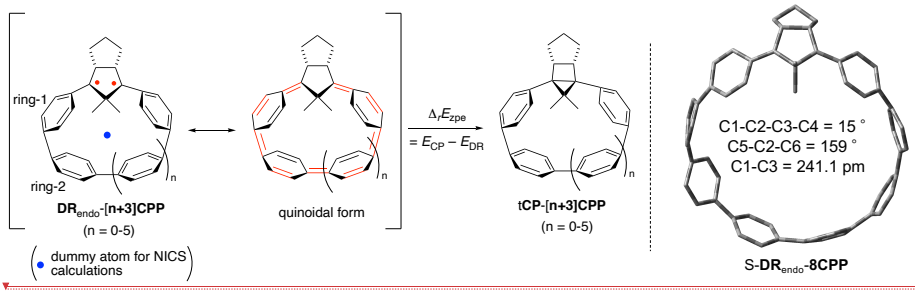

entry	DR$_{endo}$-CPP	$\Delta_r E = E_{CP} - E_{DR}$ /kcal mol^{-1} SE_{DR}/SE_{CP}	$\Delta E_{ST} = E_S - E_T$ /kcal mol^{-1}	occupation number in HOMO/LUMO[a]	HOMA (benzene distortion (bent) angle (α, °)) ring-1 singlet	ring-1 triplet	ring-2 singlet	ring-2 triplet	NICS(0)$_{zz}$ (NICS(0)$_{iso}$)[b] singlet	triplet
1	DR$_{endo}$-3CPP	– 101.0/–	−21.30	1.91/0.09	0.465 (31.8)	0.751 (26.9)	0.541 (30.0)	0.990 (19.3)	−3.6 (−5.5)	+11.9 (−0.8)
2	DR$_{endo}$-4CPP	−25.6 103.0/95.6	−4.50	1.64/0.36	0.876 (18.5)	0.888 (18.8)	0.971 (18.4)	0.990 (17.2)	−19.2 (−11.1)	+10.4 (−1.0)
3	DR$_{endo}$-5CPP	−31.5 92.3/79.0	−1.90	1.54/0.46	0.942 (13.3)	0.930 (14.2)	0.993 (12.7)	0.994 (12.6)	−2.9 (−5.2)	+5.2 (−2.3)
4	DR$_{endo}$-6CPP	−32.5 82.6/68.3	−1.77	1.47/0.53	0.951 (11.8)	0.940 (12.3)	0.995 (9.5)	0.995 (9.7)	+0.1 (−3.5)	+3.6 (−2.2)
5	DR$_{endo}$-7CPP	−35.6 78.2/60.8	+0.13	1.16/0.84	0.968 (12.1)	0.966 (12.3)	0.995 (8.5)	0.995 (8.6)	+2.4 (−2.1)	+2.9 (−2.0)
6	DR$_{endo}$-8CPP	−35.0 70.9/54.1	+0.19	1.12/0.88	0.963 (10.7)	0.963 (10.7)	0.995 (8.0)	0.995 (8.1)	+2.1 (−1.7)	+2.3 (−1.6)

[a] Occupation numbers in HOMO/LUMO were determined at the CASSCF(2,2)//BS-UCAM-B3LYP/6-31G(d) level of theory. [b] NICS values at the ring centers were computed at the UCAM-B3LYP/6-31 + G(d) level of theory.

削除: xo

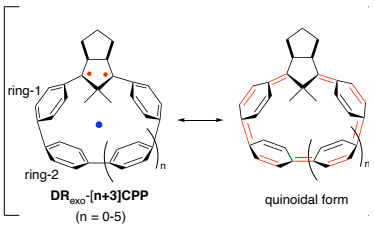

削除:

削除: DR$_{exo}$

削除: b

削除: ↵ ... [5]

書式を変更: フォント：斜体，上付き

削除: 10.3

削除: exo

削除: 579

削除: 776

削除: 644

削除: 973

削除: 14.7

削除: 15

削除: ↵ ... [6]

削除: 91.3

削除: 16.0

削除: 14.1

削除: 15.7

削除: 10.8

削除: 8.8

削除: 0.8

削除: 6.6

削除: 29.3

削除: exo

削除: 842

削除: 865

削除: 913

削除: 977

削除: 5

削除: 6.58

削除: 75…0.3625↵ ... [8]

削除: 96.0…03.0/88.0 ... [7]

削除: 9.9

削除: 10.2

削除: 11.7

削除: 9.3

The quinoidal structure of S-**DR**$_{endo}$**-CPP** was evaluated using the harmonic oscillator model of aromaticity (HOMA),[74] which was determined from the bond distances computed in the curved paraphenylene moieties. As shown in entries 1 and 2, the HOMA values of "ring-1" and "ring-2" in the singlet state of **DR**$_{endo}$**-3CPP** were found to be significantly smaller than 1.0. As the ring size increased (entries 1–6), the HOMA values approached 1.0. In contrast to the small HOMA values in the singlet states, the corresponding values for the triplet states were found to be much larger than those in the singlet states, even for **DR**$_{endo}$**-3CPP** (entry 1). Thus, the singlet state of **DR**$_{endo}$**-3CPP** possesses a significant bond-alternated quinoidal form. We realized that the quinoidal structure of the singlet state of S-**DR**$_{endo}$**-(n+3)CPPs** would show in-plane aromaticity[75–79] when the homoconjugation[80,81] of two radical sites exists in the macrocyclic structures. The nucleus-independent chemical shift values, NICS(0)$_{zz}$ and NICS(0)$_{iso}$,[82–84] at the center of the ring for the singlet and triplet states were computed to examine the in-plane aromaticity (Table 3). Interestingly, the NICS values were prone to become negative with decreasing the ring size of the singlet state, indicating the in-plane aromaticity emerges in the small size S-**DR**$_{endo}$**-(n+3)CPP**s. The NICS value of S-**DR**$_{endo}$**-4CPP**, NICS(0)$_{zz}$ (NICS(0)$_{iso}$), was highly negative, –19.2 (–11.1), although the NICS value of the triplet state was found to be +10.4 (–1.0) (entry 2, Figure 10a). The in-plane aromaticity of S-**DR**$_{endo}$**-4CPP** was clearly visualized using anisotropy of the induced current density (ACID)[85] plots (Figures 10b and 10c) and 2D-NICS plots (Figures 10d,e). The smaller negative NICS value of S-**DR**$_{endo}$**-3CPP** than that of S-**DR**$_{endo}$**-4CPP** is rationalized by the large bond alternation of the quinoidal structures, which

削除：**DR**$_{exo}$

削除：

削除：29.3

削除：14.2

削除：10.5

削除：1.8

is reflected by the low degree of π-conjugation. As found in the CASSCF calculations, the diradical character increases with increasing the ring size. Thus, the in-plane aromaticity becomes low for the larger sized S-**DR**$_{endo}$ (*n*+3)**CPP**s.

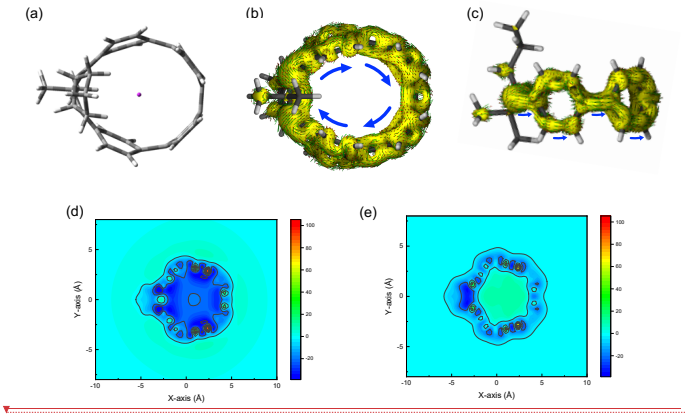

Figure 10. Molecular structure of S-**DR**$_{endo}$**-4CPP** with dummy atom at the ring center (a). Top view (b) and side view (c) of the ACID plot of the ring current in S-**DR**$_{endo}$**-4CPP**. 2D-NICS(0)$_{zz}$ plot for S-**DR**$_{endo}$**-4CPP** (d) and T-**DR**$_{endo}$**-4CPP** (e).

削除:

削除: exo

削除: exo

Conclusion

In this study, a novel azoalkane, **AZ-6CPP** that is the precursor of **DR-6CPP**, was synthesized. A relatively high fluorescence quantum yield of 79% was observed for **AZ-6CPP** because the embedded azo moiety turned on the HOMO–LUMO absorption and emission in the small CPPs via symmetry breaking. The photochemical denitrogenation **AZ-6CPP** was carried out to produce the ring-close

削除: able to be

compound t**CP-6CPP**. The intermediary diradical **DR$_{endo}$-6CPP** was directly detected using EPR spectroscopy analysis under low-temperature matrix isolation conditions. A singlet ground state was revealed by EPR experiments, although the parent diradical, **DR-2Ph**, has a triplet ground state. The singlet ground state of **DR$_{endo}$-6CPP** is rationalized as having a puckered structure in the diradical unit, induced by the curved structure of the paraphenylene moiety. A computational study on the effects of size on the chemistry of **DR$_{endo}$-(*n*+3)CPP** (*n* = 0–5) demonstrated that (1) the ground state spin-multiplicity is largely dependent on the ring size, and the singlet ground state was favored for (3–6)CPP derivatives, (2) in-plane aromaticity emerged for small singlet states such as **DR$_{endo}$-4CPP**, which involves homoconjugation in the 1,3-diradical moiety, and (3) S-**DR$_{endo}$-3CPP** is proposed to possess a closed-shell quinoidal structure due to the strongly curved paraphenylene units. The singlet ground state of small-sized diradicals **DR-(*n*+3)CPP** was experimentally proved by the generation of **DR-6CPP** from **AZ-6CPP**.

書式を変更：下付き

書式を変更：下付き

削除：7

削除：The synthesis of azo compounds featuring various ring sizes is awaited to examine the theoretical predictions.

Supporting Information

This Supporting Information is available free of charge at

Experimental and theoretical details (PDF)

Crystallographic data for **AZ-6CPP** (CIF)

Acknowledgements

Mass spectrometry measurements were performed at the Natural Science Center for Basic Research and Development (N-BARD) of Hiroshima University. This work was by JSPS KAKENHI Grant

Numbers 17H03022 (MA), 20K21197 (MA), and 16H06352 (SY), and also supported by the International Collaborative Research Program of Institute for Chemical Research, Kyoto University (grant 2020-43).

References

(1) Ai, X.; Evans, E. W.; Dong, S.; Gillett, A. J.; Guo, H.; Chen, Y.; Hele, T. J. H.; Friend, R. H.; Li, F. Efficient Radical-Based Light-Emitting Diodes with Doublet Emission. *Nature* **2018**, *563* (7732), 536–540. https://doi.org/10.1038/s41586-018-0695-9.

(2) Hattori, Y.; Kusamoto, T.; Nishihara, H. Luminescence, Stability, and Proton Response of an Open-Shell (3,5- Dichloro-4-Pyridyl)Bis(2,4,6-Trichlorophenyl)Methyl Radical. *Angew. Chemie - Int. Ed.* **2014**, *53* (44), 11845–11848. https://doi.org/10.1002/anie.201407362.

(3) Liu, C.; Hamzehpoor, E.; Sakai-Otsuka, Y.; Jadhav, T.; Perepichka, D. F. 90% Quantum Yield Pure-Red Doublet Emission from Stable, Colorless, Iodinated Triphenylmethane Solid. *Angew. Chemie Int. Ed.* **2020**, 1–6. https://doi.org/10.1002/anie.202009867.

(4) Tang, S.; Zhang, L.; Ruan, H.; Zhao, Y.; Wang, X. A Magnetically Robust Triplet Ground State Sulfur-Hydrocarbon Diradical Dication. *9*, 2020. https://doi.org/10.1021/jacs.0c02141.

(5) Gallagher, N. M.; Olankitwanit, A.; Rajca, A. High-Spin Organic Molecules. *J. Org. Chem.* **2015**, *80* (3), 1291–1298. https://doi.org/10.1021/jo502505r.

(6) Kyushin, S.; Kurosaki, Y.; Otsuka, K.; Imai, H.; Ishida, S.; Kyomen, T.; Hanaya, M.;

Matsumoto, H. Silicon–Silicon π Single Bond. *Nat. Commun.* **2020**, *11* (1), 1–7. https://doi.org/10.1038/s41467-020-17815-z.

(7) Yildiz, C. B.; Leszczyńska, K. I.; González-Gallardo, S.; Zimmer, M.; Azizoglu, A.; Biskup, T.; Kay, C. W. M.; Huch, V.; Rzepa, H. S.; Scheschkewitz, D. Equilibrium Formation of Stable All-Silicon Versions of 1,3-Cyclobutanediyl. *Angew. Chemie - Int. Ed.* **2020**, *59* (35), 15087–15092. https://doi.org/10.1002/anie.202006283.

(8) Nukazawa, T.; Iwamoto, T. An Isolable Tetrasilicon Analogue of a Planar Bicyclo[1.1.0]Butane with π-Type Single-Bonding Character. *J. Am. Chem. Soc.* **2020**, *142* (22), 9920–9924. https://doi.org/10.1021/jacs.0c03874.

(9) Akisaka, R.; Abe, M. Kinetic Stabilization of Localized Singlet Diradicaloids With π Single Bonding Character. In *Kinetic Control in Synthesis and Self-Assembly*; Elsevier, 2019; pp 1–20. https://doi.org/10.1016/B978-0-12-812126-9.00001-8.

(10) Akisaka, R.; Abe, M. Bulky Substituent Effect on Reactivity of Localized Singlet Cyclopentane-1,3-diyls with Π-Single Bonding (C-π-C) Character. *Chem. – An Asian J.* **2019**, *14* (23), 4223–4228. https://doi.org/10.1002/asia.201901253.

(11) Abe, M.; Akisaka, R. Is π-Single Bonding (CπC) Possible? A Challenge in Organic Chemistry. *Chem. Lett.* **2017**, *46* (11), 1586–1592. https://doi.org/10.1246/cl.170711.

(12) Abe, M.; Ye, J.; Mishima, M. The Chemistry of Localized Singlet 1,3-Diradicals (Biradicals):

From Putative Intermediates to Persistent Species and Unusual Molecules with a π-Single Bonded Character. *Chem. Soc. Rev.* **2012**, *41* (10), 3808–3820. https://doi.org/10.1039/c2cs00005a.

(13) Abe, M. Diradicals. **2013**, *113*, 7011.

(14) Ullrich, T.; Pinter, P.; Messelberger, J.; Haines, P.; Kaur, R.; Hansmann, M. M.; Munz, D.; Guldi, D. M. Singlet Fission in Carbene-Derived Diradicaloids. *Angew. Chemie Int. Ed.* **2020**, *59* (20), 7906–7914. https://doi.org/10.1002/anie.202001286.

(15) Kubo, T. Recent Progress in Quinoidal Singlet Biradical Molecules. *Chem. Lett.* **2015**, *44* (2), 111–122. https://doi.org/10.1246/cl.140997.

(16) Tobe, Y. Non-Alternant Non-Benzenoid Aromatic Compounds: Past, Present, and Future. *Chem. Rec.* **2015**, *15* (1), 86–96. https://doi.org/10.1002/tcr.201402077.

(17) Dressler, J. J.; Haley, M. M. Learning How to Fine-tune Diradical Properties by Structure Refinement. *J. Phys. Org. Chem.* **2020**. https://doi.org/10.1002/poc.4114.

(18) Mori, S.; Akita, M.; Suzuki, S.; Asano, M. S.; Murata, M.; Akiyama, T.; Matsumoto, T.; Kitamura, C.; Kato, S. Open-Shell Singlet Diradicaloid Difluoreno[4,3-b:3',4'-d]Furan and Its Radical Cation and Dianion. *Chem. Commun.* **2020**, *56* (44), 5881–5884. https://doi.org/10.1039/d0cc01638a.

(19) Sahara, K.; Abe, M.; Zipse, H.; Kubo, T. Duality of Reactivity of a Biradicaloid Compound

with an O-Quinodimethane Scaffold. *J. Am. Chem. Soc.* **2020**, *142* (11), 5408–5418. https://doi.org/10.1021/jacs.0c01003.

(20) Shu, C.; Zhang, H.; Olankitwanit, A.; Rajca, S.; Rajca, A. High-Spin Diradical Dication of Chiral π-Conjugated Double Helical Molecule. *J. Am. Chem. Soc.* **2019**, *141* (43), 17287–17294. https://doi.org/10.1021/jacs.9b08711.

(21) Gallagher, N.; Zhang, H.; Junghoefer, T.; Giangrisostomi, E.; Ovsyannikov, R.; Pink, M.; Rajca, S.; Casu, M. B.; Rajca, A. Thermally and Magnetically Robust Triplet Ground State Diradical. *J. Am. Chem. Soc.* **2019**. https://doi.org/10.1021/jacs.9b00558.

(22) Ravat, P.; Šolomek, T.; Häussinger, D.; Blacque, O.; Juríček, M. Dimethylcethrene: A Chiroptical Diradicaloid Photoswitch. *J. Am. Chem. Soc.* **2018**, *140* (34), 10839–10847. https://doi.org/10.1021/jacs.8b05465.

(23) Jiang, C.; Bang, Y.; Wang, X.; Lu, X.; Lim, Z.; Wei, H.; El-Hankari, S.; Wu, J.; Zeng, Z. Tetrabenzo-Chichibabin's Hydrocarbons: Substituent Effects and Unusual Thermochromic and Thermomagnetic Behaviours. *Chem. Commun.* **2018**, *54* (19), 2389–2392. https://doi.org/10.1039/c8cc00378e.

(24) Kishi, R.; Murata, Y.; Saito, M.; Morita, K.; Abe, M.; Nakano, M. Theoretical Study on Diradical Characters and Nonlinear Optical Properties of 1,3-Diradical Compounds. *J. Phys. Chem. A* **2014**, *118* (45), 10837–10848. https://doi.org/10.1021/jp508657s.

(25) Abe, M.; Kawanami, S.; Ishihara, C.; Nojima, M. 2-Silyl Group Effect on the Reactivity of Cyclopentane-1,3-Diyls. Intramolecular Ring-Closure versus Silyl Migration. *J. Org. Chem.* **2004**, *69* (17), 5622–5626. https://doi.org/10.1021/jo049580z.

(26) Abe, M.; Kubo, E.; Nozaki, K.; Matsuo, T.; Hayashi, T. An Extremely Long-Lived Singlet 4,4-Dimethoxy-3,5-Diphenylpyrazolidine-3,5- Diyl Derivative: A Notable Nitrogen-Atom Effect on Intra- and Intermolecular Reactivity. *Angew. Chemie - Int. Ed.* **2006**, *45* (46), 7828–7831. https://doi.org/10.1002/anie.200603287.

(27) Yoshidomi, S.; Mishima, M.; Seyama, S.; Abe, M.; Fujiwara, Y.; Ishibashi, T.-A. Direct Detection of a Chemical Equilibrium between a Localized Singlet Diradical and Its σ-Bonded Species by Time-Resolved UV/Vis and IR Spectroscopy. *Angew. Chemie - Int. Ed.* **2017**, *56* (11), 2984–2988. https://doi.org/10.1002/anie.201612329.

(28) Yoshidomi, S.; Abe, M. 1,2-Diazacyclopentane-3,5-Diyl Diradicals: Electronic Structure and Reactivity. *J. Am. Chem. Soc.* **2019**, *141* (9), 3920–3933. https://doi.org/10.1021/jacs.8b12254.

(29) Stuyver, T.; Chen, B.; Zeng, T.; Geerlings, P.; De Proft, F.; Hoffmann, R. Do Diradicals Behave Like Radicals? *Chem. Rev.* **2019**, *119* (21), 11291–11351. https://doi.org/10.1021/acs.chemrev.9b00260.

(30) Xu, J. D.; Hrovat, D. A.; Borden, W. T. Ab Initio Calculations of the Potential Surfaces for the Lowest Singlet and Triplet States of 2,2-Difluorocyclopentane-1,3-Diyl. The Singlet

Diradical Lies Below the Triplet. *J. Am. Chem. Soc.* **1994**, *116* (6), 5425–5427.

(31) Jasti, R.; Bhattacharjee, J.; Neaton, J. B.; Bertozzi, C. R. Synthesis, Characterization, and Theory of [9]-, [12]-, and [18]Cycloparaphenylene: Carbon Nanohoop Structures. *J. Am. Chem. Soc.* **2008**, *130* (52), 17646–17647. https://doi.org/10.1021/ja807126u.

(32) Takaba, H.; Omachi, H.; Yamamoto, Y.; Bouffard, J.; Itami, K. Selective Synthesis of [12]Cycloparaphenylene. *Angew. Chemie Int. Ed.* **2009**, *48* (33), 6112–6116. https://doi.org/10.1002/anie.200902617.

(33) Yamago, S.; Watanabe, Y.; Iwamoto, T. Synthesis of [8]Cycloparaphenylene from a Square-Shaped Tetranuclear Platinum Complex. *Angew. Chemie Int. Ed.* **2010**, *49* (4), 757–759. https://doi.org/10.1002/anie.200905659.

(34) Iwamoto, T.; Watanabe, Y.; Sakamoto, Y.; Suzuki, T.; Yamago, S. Selective and Random Syntheses of [n]Cycloparaphenylenes (n = 8–13) and Size Dependence of Their Electronic Properties. *J. Am. Chem. Soc.* **2011**, *133* (21), 8354–8361. https://doi.org/10.1021/ja2020668.

(35) Darzi, E. R.; Jasti, R. The Dynamic, Size-Dependent Properties of [5]-[12]Cycloparaphenylenes. *Chem. Soc. Rev.* **2015**, *44* (18), 6401–6410. https://doi.org/10.1039/c5cs00143a.

(36) Li, Y.; Segawa, Y.; Yagi, A.; Itami, K. A Nonalternant Aromatic Belt: Methylene-Bridged [6]Cycloparaphenylene Synthesized from Pillar[6]Arene. *J. Am. Chem. Soc.* **2020**, *142* (29),

12850–12856. https://doi.org/10.1021/jacs.0c06007.

(37) Matsumoto, M.; Antol, I.; Abe, M. Curve Effect on Singlet Diradical Contribution in Kekulé-Type Diradicals: A Sensitive Probe for Quinoidal Structure in Curved π-Conjugated Molecules. *Molecules* **2019**, *24* (1), 209. https://doi.org/10.3390/molecules24010209.

(38) Li, P.; Sisto, T. J.; Darzi, E. R.; Jasti, R. The Effects of Cyclic Conjugation and Bending on the Optoelectronic Properties of Paraphenylenes. *Org. Lett.* **2014**, *16* (1), 182–185. https://doi.org/10.1021/ol403168x.

(39) Stratmann, R. E.; Scuseria, G. E.; Frisch, M. J. An Efficient Implementation of Time-Dependent Density-Functional Theory for the Calculation of Excitation Energies of Large Molecules. *J. Chem. Phys.* **1998**, *109* (19), 8218–8224. https://doi.org/10.1063/1.477483.

(40) Becke, A. D. Density-functional Thermochemistry. III. The Role of Exact Exchange. *J. Chem. Phys.* **1993**, *98* (7), 5648–5652. https://doi.org/10.1063/1.464913.

(41) Lee, C.; Yang, W.; Parr, R. G. Development of the Colic-Salvetti Correlation-Energy into a Functional of the Electron Density Formula Chengteh. *Phys. Rev. B* **1988**, *37*, 785–789.

(42) Evans, P. J.; Darzi, E. R.; Jasti, R. Efficient Roomerature Synthesis of a Highly Strained Carbon Nanohoop Fragment of Buckminsterfullerene. *Nat. Chem.* **2014**, *6* (5), 404–408. https://doi.org/10.1038/nchem.1888.

(43) Kayahara, E.; Patel, V. K.; Yamago, S. Synthesis and Characterization of

[5]Cycloparaphenylene. *J. Am. Chem. Soc.* **2014**, *136* (6), 2284–2287. https://doi.org/10.1021/ja413214q.

(44) Xia, J.; Jasti, R. Synthesis, Characterization, and Crystal Structure of [6]Cycloparaphenylene. *Angew. Chemie - Int. Ed.* **2012**, *51* (10), 2474–2476. https://doi.org/10.1002/anie.201108167.

(45) Lovell, T. C.; Colwell, C. E.; Zakharov, L. N.; Jasti, R. Symmetry Breaking and the Turn-on Fluorescence of Small, Highly Strained Carbon Nanohoops. *Chem. Sci.* **2019**, *10* (13), 3786–3790. https://doi.org/10.1039/c9sc00169g.

(46) Suenobu, T.; Arahori, I.; Nakayama, K. I.; Suzuki, T.; Katoh, R.; Nakagawa, T. Reaction of Oxygen with the Singlet Excited State of [n]Cycloparaphenylenes (n = 9, 12, and 15): A Time-Resolved Transient Absorption Study Seamlessly Covering Time Ranges from Subnanoseconds to Microseconds by the Randomly-Interleaved-Pulse-Train Method. *J. Phys. Chem. A* **2020**, *124* (1), 46–55. https://doi.org/10.1021/acs.jpca.9b09846.

(47) Tanaka, F.; Tsumura, K.; Furuta, T.; Iwamoto, K.; Okamoto, M. Efficiencies of Singlet Oxygen Production and Rate Constants for Oxygen Quenching in the S1 State of Dicyanonaphthalenes and Related Compounds. *Photochem. Photobiol. Sci.* **2007**, *7* (1), 56–62. https://doi.org/10.1039/b711781g.

(48) Nakagawa, T.; Okamoto, K.; Hanada, H.; Katoh, R. Probing with Randomly Interleaved Pulse Train Bridges the Gap between Ultrafast Pump-Probe and Nanosecond Flash Photolysis. *Opt. Lett.* **2016**, *41* (7), 1498–1501. https://doi.org/10.1364/OL.41.001498.

(49) Adam, W.; Nau, W. M.; Fragale, G.; Wirz, J.; Klapstein, D. Phosphorescence and Transient Absorption of Azoalkane Triplet States. *J. Am. Chem. Soc.* **1995**, *117* (50), 12578–12592. https://doi.org/10.1021/ja00155a022.

(50) Eaton, S. S.; More, K. M.; Sawant, B. M.; Eaton, G. R. Use of the EPR Half-Field Transition To Determine the Interspin Distance and the Orientation of the Interspin Vector in Systems with Two Unpaired Electrons. *J. Am. Chem. Soc.* **1983**, *105* (22), 6560–6567. https://doi.org/10.1021/ja00360a005.

(51) Adam, W.; Kita, F.; Harrer, H. M.; Nau, W. M.; Zipf, R. The D Parameter (EPR Zero-Field Splitting) of Localized 1,3-Cyclopentanediyl Triplet Diradicals as a Measure of Electronic Substituent Effects on the Spin Densities in Para-Substituted Benzyl-Type Radicals. *J. Org. Chem.* **1996**, *61* (20), 7056–7065. https://doi.org/10.1021/jo960396q.

(52) Adam, W.; Van Barneveld, C.; Emmert, O. The EPR D Parameter as a Measure of Spin Delocalization in Cyclopentane-1,3-Diyl Triplet Diradicals with Extended Conjugation π-Type Substituents. *J. Chem. Soc. Perkin Trans. 2* **2000**, No. 4, 637–641. https://doi.org/10.1039/a909845c.

(53) Sinnecker, S.; Neese, F. Spin-Spin Contributions to the Zero-Field Splitting Tensor in Organic Triplets, Carbenes and Biradicals - A Density Functional and Ab Initio Study. *J. Phys. Chem. A* **2006**, *110* (44), 12267–12275. https://doi.org/10.1021/jp0643303.

(54) Neese, F. Calculation of the Zero-Field Splitting Tensor on the Basis of Hybrid Density

Functional and Hartree-Fock Theory. *J. Chem. Phys.* **2007**, *127* (16). https://doi.org/10.1063/1.2772857.

(55) Neese, F. The ORCA Program System. *Wiley Interdiscip. Rev. Comput. Mol. Sci.* **2012**, *2* (1), 73–78. https://doi.org/10.1002/wcms.81.

(56) Neese, F. Software Update: The ORCA Program System, Version 4.0. *Wiley Interdiscip. Rev. Comput. Mol. Sci.* **2018**, *8* (1), 4–9. https://doi.org/10.1002/wcms.1327.

(57) Buchwalter, S. L.; Gloss, G. L. An Electron Spin Resonance Study of Matrix Isolated 1,3-Cyclopentadiyl, a Localized 1,3-Carbon Biradical. *J. Am. Chem. Soc.* **1975**, *97* (13), 3857–3858. https://doi.org/10.1021/ja00846a073.

(58) Wang, Z.; Akisaka, R.; Yabumoto, S.; Nakagawa, T.; Hatano, S.; Abe, M. Impact of the Macrocyclic Structure and Dynamic Solvent Effect on the Reactivity of a Localised Singlet Diradicaloid with π-Single Bonding Character. *Chem. Sci.* **2020**, No. Scheme 1. https://doi.org/10.1039/d0sc05311b.

(59) Adam, W.; Maas, W.; Nau, W. M. Wavelength-Selective Photodenitrogenation of Azoalkanes to High-Spin Polyradicals with Cyclopentane-1,3-Diyl Spin-Carrying Units and Their Photobleaching: EPR/UV Spectroscopy and Product Studies of the Matrix-Isolated Species. *J. Org. Chem.* **2000**, *65* (25), 8790–8796. https://doi.org/10.1021/jo0013960.

(60) Bleaney, Brebis and Bowers, K. D. Anomalous Paramagnetism of Copper Acetate.

Proceeding R. Soc. A **1952**, *214*, 451–465.

(61) Yanai, T.; Tew, D. P.; Handy, N. C. A New Hybrid Exchange–Correlation Functional Using the Coulomb-Attenuating Method (CAM-B3LYP). *Chem. Phys. Lett.* **2004**, *393* (1–3), 51–57. https://doi.org/10.1016/j.cplett.2004.06.011.

(62) Hegarty, D.; Robb, M. A. Application of Unitary Group Methods to Configuration Interaction Calculations. *Mol. Phys.* **1979**, *38* (6), 1795–1812. https://doi.org/10.1080/00268977900102871.

(63) M. J. Frisch, G. W. Trucks, H. B. Schlegel, G. E. Scuseria, M. A. Robb, J. R. Cheeseman, G. Scalmani, V. Barone, G. A. Petersson, H. Nakatsuji, X. Li, M. Caricato, A. V. Marenich, J. Bloino, B. G. Janesko, R. Gomperts, B. Mennucci, H. P. Hratchian, J. V. , 2016. No Title. 2016.

(64) Yamaguchi, K.; Jensen, F.; Dorigo, A.; Houk, K. N. A Spin Correction Procedure for Unrestricted Hartree-Fock and Møller-Plesset Wavefunctions for Singlet Diradicals and Polyradicals. *Chem. Phys. Lett.* **1988**, *149* (5–6), 537–542. https://doi.org/10.1016/0009-2614(88)80378-6.

(65) Andersson, K. Different Forms of the Zeroth-Order Hamiltonian in Second-Order Perturbation Theory with a Complete Active Space Self-Consistent Field Reference Function. *Theor. Chim. Acta* **1995**, *91* (1–2), 31–46. https://doi.org/10.1007/BF01113860.

(66) Hoffmann, R. Interaction of Orbitals through Space and through Bonds. *Acc. Chem. Res.* **1971**, *4* (1), 1–9. https://doi.org/10.1021/ar50037a001.

(67) Hoffmann, R. Trimethylene and the Addition of Methylene to Ethylene. *J. Am. Chem. Soc.* **1968**, *90* (6), 1475–1485. https://doi.org/10.1021/ja01008a016.

(68) Abe, M.; Ishihara, C.; Nojima, M. DFT Prediction of Ground-State Spin Multiplicity of Cyclobutane-1,3-Diyls: Notable Effects of Two Sets of through-Bond Interactions. *J. Org. Chem.* **2003**, *68* (4), 1618–1621. https://doi.org/10.1021/jo026345c.

(69) Abe, M.; Ishihara, C.; Tagegami, A. Theoretical Calculations of the Effects of 2-Heavier Group 14 Element and Substituents on the Singlet-Triplet Energy Gap in Cyclopentane-1,3-Diyls and Computational Prediction of the Reactivity of Singlet 2-Silacyclopentane-1,3-Diyls. *J. Org. Chem.* **2004**, *69* (21), 7250–7255. https://doi.org/10.1021/jo0490447.

(70) Borden, W. T. Effects of Electron Donation into C-F Σ* Orbitals: Explanations, Predictions and Experimental Tests. *Chem. Commun.* **1998**, No. 18, 1919–1925. https://doi.org/10.1039/a803750g.

(71) https://gitlab.com/Molcas/OpenMolcas.

(72) Nakagaki, T.; Sakai, T.; Mizuta, T.; Fujiwara, Y.; Abe, M. Kinetic Stabilization and Reactivity of π Single-Bonded Species: Effect of the Alkoxy Group on the Lifetime of Singlet 2,2-Dialkoxy-1,3- Diphenyloctahydropentalene-1,3-Diyls. *Chem. - A Eur. J.* **2013**, *19* (31),

10395–10404. https://doi.org/10.1002/chem.201300038.

(73) Segawa, Y.; Omachi, H.; Itami, K. Theoretical Studies on the Structures and Strain Energies of Cycloparaphenylenes. *Org. Lett.* **2010**, *12* (10), 2262–2265. https://doi.org/10.1021/ol1006168.

(74) Krygowski, T. M.; Cyrański, M. K. Structural Aspects of Aromaticity. *Chem. Rev.* **2001**, *101* (5), 1385–1419. https://doi.org/10.1021/cr990326u.

(75) Rickhaus, M.; Jirasek, M.; Tejerina, L.; Gotfredsen, H.; Peeks, M. D.; Haver, R.; Jiang, H. W.; Claridge, T. D. W.; Anderson, H. L. Global Aromaticity at the Nanoscale. *Nat. Chem.* **2020**, *12* (3), 236–241. https://doi.org/10.1038/s41557-019-0398-3.

(76) Peeks, M. D.; Gong, J. Q.; McLoughlin, K.; Kobatake, T.; Haver, R.; Herz, L. M.; Anderson, H. L. Aromaticity and Antiaromaticity in the Excited States of Porphyrin Nanorings. *J. Phys. Chem. Lett.* **2019**, *10* (8), 2017–2022. https://doi.org/10.1021/acs.jpclett.9b00623.

(77) Schleyer, P. von R.; Jiao, H.; Hommes, N. J. R. van E.; Malkin, V. G.; Malkina, O. L. An Evaluation of the Aromaticity of Inorganic Rings: Refined Evidence from Magnetic Properties. *J. Am. Chem. Soc.* **1997**, *119* (51), 12669–12670. https://doi.org/10.1021/ja9719135.

(78) Burley, G. A. Trannulenes with “in-Plane” Aromaticity: Candidates for Harvesting Light Energy. *Angew. Chem. Int. Ed.* **2005**, *44*. https://doi.org/10.1002/anie.200500362.

(79) Toriumi, N.; Muranaka, A.; Kayahara, E.; Yamago, S.; Uchiyama, M. In-Plane Aromaticity in Cycloparaphenylene Dications: A Magnetic Circular Dichroism and Theoretical Study. *J. Am. Chem. Soc.* **2015**, *137* (1), 82–85. https://doi.org/10.1021/ja511320f.

(80) Williams, R. V. Homoaromaticity. *Chem. Rev.* **2001**, *101* (5), 1185–1204. https://doi.org/10.1021/cr9903149.

(81) winstein, S.; Sonnenberg, J.; deVries, L. Homo-Aromatic Structures. *J. Am. Chem. Soc.* **1959**, *81* (24), 6524–6525. https://doi.org/10.1021/ja01533a052.

(82) Schleyer, P. vo. R.; Maerker, C.; Dransfeld, A.; Jiao, H.; Hommes, N. J. R. V. E. Nucleus-Independent Chemical Shifts : A Simple and Efficient Aromaticity Probe. *Jouranal Am. Chem. Soc.* **1996**, *118* (26), 6317–6318.

(83) Steiner, E.; Fowler, P. W.; Jenneskens, L. W. Counter-Rotating Ring Currents in Coronene and Corannulene. *Angew. Chemie - Int. Ed.* **2001**, *40* (2), 362–366. https://doi.org/10.1002/1521-3773(20010119)40:2<362::AID-ANIE362>3.0.CO;2-Z.

(84) Fallah-Bagher-Shaidaei, H.; Wannere, C. S.; Corminboeuf, C.; Puchta, R.; Schleyer, P. V. R. Which NICS Aromaticity Index for Planar π Rings Is Best? *Org. Lett.* **2006**, *8* (5), 863–866. https://doi.org/10.1021/ol0529546.

(85) Geuenich, D.; Hess, K.; Köhler, F.; Herges, R. Anisotropy of the Induced Current Density (ACID), a General Method to Quantify and Visualize Electronic Delocalization. *Chem. Rev.*

2005, *105* (10), 3758–3772. https://doi.org/10.1021/cr0300901.

ページ 22: [1] 削除　　安倍　学　　2021/03/10 18:08:00

ページ 22: [1] 削除　　安倍　学　　2021/03/10 18:08:00

ページ 22: [1] 削除　　安倍　学　　2021/03/10 18:08:00

ページ 22: [1] 削除　　安倍　学　　2021/03/10 18:08:00

ページ 22: [1] 削除　　安倍　学　　2021/03/10 18:08:00

ページ 22: [2] 削除　　安倍　学　　2021/03/06 8:55:00

ページ 22: [2] 削除　　安倍　学　　2021/03/06 8:55:00

ページ 22: [2] 削除　　安倍　学　　2021/03/06 8:55:00

ページ 22: [2] 削除　　安倍　学　　2021/03/06 8:55:00

ページ 22: [2] 削除　　安倍　学　　2021/03/06 8:55:00

ページ 22: [2] 削除　　安倍　学　　2021/03/06 8:55:00

ページ 22: [2] 削除　　安倍　学　　2021/03/06 8:55:00

ページ 22: [2] 削除　　安倍　学　　2021/03/06 8:55:00

ページ 22: [2] 削除　　安倍　学　　2021/03/06 8:55:00

ページ 22: [2] 削除　　安倍　学　　2021/03/06 8:55:00

ページ 22: [2] 削除　　安倍　学　　2021/03/06 8:55:00

ページ 22: [2] 削除　　安倍　学　　2021/03/06 8:55:00

ページ 22: [2] 削除　　安倍　学　　2021/03/06 8:55:00

ページ 22: [2] 削除　　安倍　学　　2021/03/06 8:55:00

ページ 22: [2] 削除　　安倍　学　　2021/03/06 8:55:00

ページ 22: [2] 削除　　安倍　学　　2021/03/06 8:55:00

ページ 22: [2] 削除　　安倍　学　　2021/03/06 8:55:00

ページ 22: [2] 削除　　安倍　学　　2021/03/06 8:55:00

ページ 22: [2] 削除　　安倍　学　　2021/03/06 8:55:00

ページ 22: [2] 削除　　安倍　学　　2021/03/06 8:55:00

ページ 22: [2] 削除　　安倍　学　　2021/03/06 8:55:00

ページ 22: [2] 削除　　安倍　学　　2021/03/06 8:55:00

ページ 22: [3] 削除　　安倍　学　　2021/03/06 9:39:00

ページ 22: [3] 削除　　安倍　学　　2021/03/06 9:39:00

ページ 22: [3] 削除　　安倍　学　　2021/03/06 9:39:00

ページ 28: [4] 削除　安倍　学　2021/03/11 9:54:00

ページ 31: [5] 削除　安倍　学　2021/03/11 18:59:00

ページ 31: [6] 削除　安倍　学　2021/03/11 18:59:00

ページ 31: [7] 削除　安倍　学　2021/03/13 14:57:00

ページ 31: [7] 削除　安倍　学　2021/03/13 14:57:00

ページ 31: [8] 削除　安倍　学　2021/03/11 18:55:00

ページ 31: [8] 削除　安倍　学　2021/03/11 18:55:00

ページ 31: [9] 削除　安倍　学　2021/03/13 14:57:00

ページ 31: [9] 削除　安倍　学　2021/03/13 14:57:00

ページ 31: [10] 削除　安倍　学　2021/03/11 19:10:00

ページ 31: [10] 削除　安倍　学　2021/03/11 19:10:00

ページ 31: [10] 削除	安倍　学	2021/03/11 19:10:00
ページ 31: [11] 削除	安倍　学	2021/03/13 14:57:00
ページ 31: [11] 削除	安倍　学	2021/03/13 14:57:00
ページ 31: [12] 削除	安倍　学	2021/03/11 19:00:00
ページ 31: [12] 削除	安倍　学	2021/03/11 19:00:00
ページ 31: [13] 削除	安倍　学	2021/03/13 14:57:00
ページ 31: [13] 削除	安倍　学	2021/03/13 14:57:00
ページ 31: [14] 削除	安倍　学	2021/03/11 19:38:00
ページ 31: [14] 削除	安倍　学	2021/03/11 19:38:00
ページ 31: [14] 削除	安倍　学	2021/03/11 19:38:00

ページ 31: [15] 削除	安倍　学	2021/03/13 14:57:00
ページ 31: [15] 削除	安倍　学	2021/03/13 14:57:00
ページ 31: [15] 削除	安倍　学	2021/03/13 14:57:00
ページ 31: [16] 削除	安倍　学	2021/03/11 20:02:00
ページ 31: [16] 削除	安倍　学	2021/03/11 20:02:00
ページ 31: [17] 削除	安倍　学	2021/03/11 18:59:00